National and Kapodistrian
University of Athens
Physics Department
Section of Condensed Matter Physics

Solution of the tight-binding Bogoliubov-de Gennes equations for topological superconductivity

A thesis written in partial fulfillment of the requirements for the completion of the Postgraduate Studies Program Materials Physics of the Physics Department's Condensed Matter Physics Section.

Written by
Rigas Spyridon

Supervised by
Prof. P. Mavropoulos
Prof. S. Blügel
Prof. D. Frantzeskakis

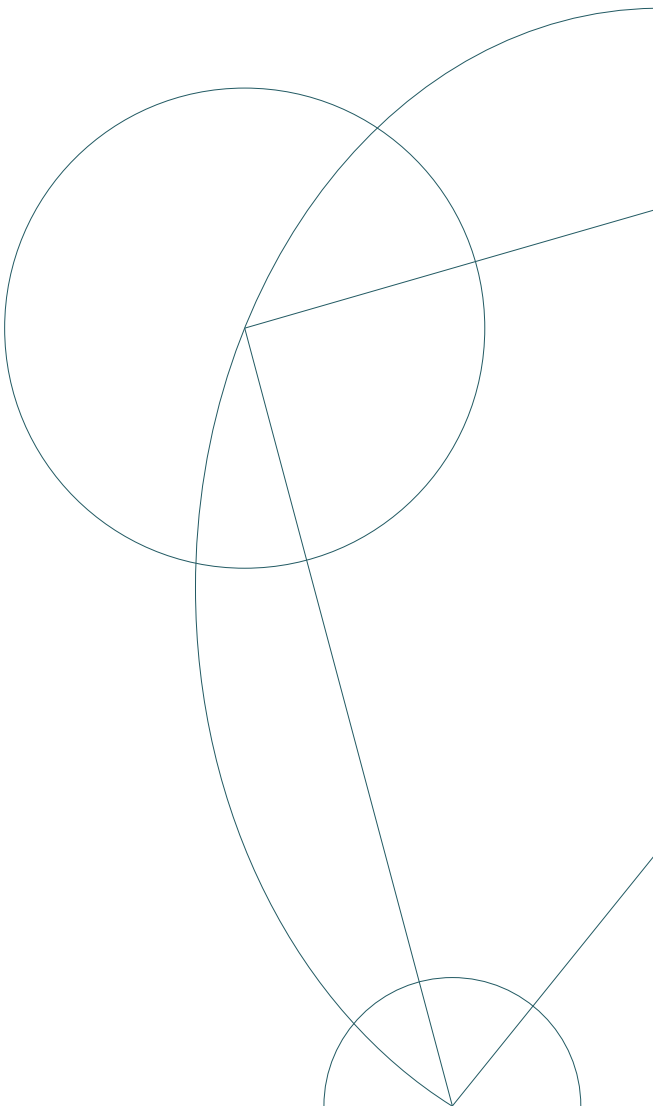

February 2021

And I don't bother anymore to lift my head toward the bright skies. If the stars are far, if the earth is small, I don't care at all, I don't mind. I want you to know that I find more astonishing, more powerful, more mysterious and gigantic, this man stopped on his way and chained.

N. Hikmet

Abstract

The field of topological materials has greatly flourished over the past few decades, ever since the shift of interest towards topological phases in condensed matter physics. Topological superconductors are an example of systems whose non-trivial topology leads to the emergence of exotic excitations as boundary modes. These modes are known as Majorana quasiparticles and their significance stems from them being equal superpositions of holes and particles, as well as the fact that they obey non-Abelian statistics. Theoretical studies on systems that can be realized as topological superconductors are fueled by the fact that the experimental observation of Majorana excitations would lead to tremendous technological advancements, such as the development of low-decoherence quantum computers.

In the first part of this thesis we review the main aspects of the tight-binding Bogoliubov-de Gennes theory of superconductivity and how the formalism of Green functions can be applied in order to study the effects of impurities within this framework. We then model superconducting surfaces and investigate how the gap's properties are affected by the presence of single non-magnetic and magnetic impurities. After observing that magnetic impurities induce bound states inside the superconducting gap, in the second part of this thesis we consider chains of magnetic atoms embedded in or adsorbed on the surface. Our findings indicate that for configurations where the magnetic chain forms a spin helix, a topologically non-trivial phase exists for the system, with localized Majorana zero modes emerging inside the spectral gap. We then perform simulations with such chains in order to investigate how this topological phase is affected by parameters such as the chain's length, or the spin helix's rotation angle, and understand some of the conditions that must be met in order to realize this topological superconductor.

Acknowledgements

The completion of the present thesis would not have been possible were it not for some people to whom I owe my heartfelt gratitude.

First and foremost, I would like to express my appreciation for my supervisor, Prof. Phivos Mavropoulos. I can't say that his door was always open, since, more often than not, the locking mechanism would malfunction and keep him locked inside his office. However, that never stopped him from being the most influential teacher I've ever interacted with, an irreplaceable mentor during the past years, an inspiring scientist and a role model for various aspects of life.

I am indebted to Prof. Stefan Blügel and Prof. Dimitri Frantzeskakis for taking the time to evaluate this thesis as committee members. I am also grateful to Dr. Philipp Rüßmann for the enlightening discussions we had on superconductivity.

Special thanks are in order for my office mates Adamantia Kosma, Dr. Petros Pantazopoulos and Apostolos Paliovaios, as well as the whole YBCO club, for bringing fun and humour into our work environment.

This project would have been nothing but fiction, were it not for the patience and untiring support from my friends and Penelope, whose company was always a safe haven. My gratitude is also extended to all my friends in the cyber-cognitariat.

Last but not least, I would like to thank my parents, cousin and especially my sister, to whom this thesis is dedicated, for their unconditional love and support throughout my life.

Contents

1 Introduction

One of the objectives of condensed matter physics is to describe and predict the physical properties of many-electron systems, an endeavour which requires a good understanding of the correlations among the systems' observables. The essence of these correlations can be captured by effective theories concerning the degrees of freedom that are associated with the system's low-energy excitations and the cornerstone of such effective theories in traditional condensed matter physics is Landau's Fermi liquid theory [1]. The main idea is that the interacting many-body problem can be simplified by making a one-to-one correspondence of the interacting electrons with effectively non-interacting quasiparticles with renormalized parameters, such as mass or velocity. In general, these quasiparticles have properties that are strikingly different from the properties of the system's original constituents, however they are governed by much simpler laws. An example [2] demonstrating the success of this method is the approach of superconductivity which reproduces the results of the BCS theory [3] by focusing on quasiparticle excitations, instead of the Cooper pairs' interactions.

Another recurring theme in condensed matter physics concerns the discovery and classification of distinctive states of matter which are characterized by a local order parameter. Once variables such as temperature or pressure cross a certain threshold, a system's properties may be qualitatively altered due to the spontaneous breaking of one or more of its symmetries. The system is then said to undergo a phase transition, which is signalled by non-analyticity in the order parameter's functional dependence of those variables. Superconductivity once again provides us with one such example, since metals can become superconducting upon lowering their temperatures below a critical point. The most widespread method of investigating the effect of symmetry breaking on order parameters is the Ginzburg-Landau [4] theory of phase transitions.

Together, the theory of the Fermi liquid and the Ginzburg-Landau theory of symmetry breaking were considered to be the holy grail of condensed matter physics, due to their triumph in explaining a series of interacting many-body problems. However, this viewpoint changed after the groundbreaking discovery of the quantum Hall effect (QHE) [5]. The observation of the QHE could not be linked to the breaking of a symmetry and therefore the state responsible for it could not be characterized by a local order parameter. It soon became evident that the distinctiveness of QHE states stems from their topology being different from that of their environment [6].

In mathematics, topology is a concept used to study the properties that remain invariant under continuous deformations of certain objects. In condensed matter physics, topology concerns the ground state properties of systems with a spectral gap that remain invariant under adiabatic deformations of their Hamiltonian[7]. Two gapped ground states are topologically equivalent if there exists an adiabatic interpolation between their respective Hamiltonians, such that the spectral gap above the ground state is preserved for all Hamiltonians along the interpolation. However, if the system's spectral gap vanishes at some point, it may undergo what is known as a topological quantum phase transition. This leads to an intrinsically quantum mechanical classification of different phases of matter, characterized by different sets of topological invariants, similarly to the characterization of phases via order parameters in the Ginzburg-Landau theory. For topologically equivalent phases, the topological invariants assigned to them assume the same value, while a system's topological phase transition is signalled by a change in the value of the corresponding topological invariant.

The QHE proved to be the spark that would lead to a paradigm shift in condensed matter physics and pave the way for what has come to be known as the field of topological materials: topological insulators[8,9], Weyl semimetals[10], topological superconductors[11] (TSCs), to name but a few. When it comes to observables, topologically non-trivial phases of matter are inextricably linked to the appearance of exotic bound states at the studied system's boundaries. TSCs, the study of which is the main purpose of this thesis, are adiabatically distinct from the Bose-Einstein condensate of Cooper pairs, which forms a topologically trivial superconducting state, because they host Majorana zero modes (MZMs). In particle physics, Majorana fermions are elementary particles which are their own anti-particles[12,13]. The condensed matter physics analogue to Majorana fermions are Majorana quasiparticle excitations which are represented as an equal superposition of electron and hole components, hence superconducting systems provide a natural hunting ground for such excitations. An additional feature of Majorana excitations is that they correspond to non-Abelian anyons; under their exchange, the system's wavefunction does not simply acquire a phase factor, but can change to a completely different quantum state[14].

Apart from their vast theoretical interest, the search for Majorana quasiparticles is also fuelled by their potential for revolutionary technological applications. The biggest obstacle in the present attempts to develop quantum computers is the decoherence induced because of the interaction of the quantum computer's qubits with their environment. Since the MZMs that appear as excitations in TSCs correspond to a single highly non-local fermionic state, this state is topologically protected from local perturbations affecting only one of its Majorana constituents. Such states can therefore be utlized as low-decoherence topological qubits for fault-tolerant quantum computers[14]. Furthermore, the state of these qubits can be controllably manipulated by adiabatically exchanging the positions of the Majorana modes, a process known as braiding, owing to their non-Abelian statistics[15].

Over the past decade and a half, pioneering discoveries have been made in the field of topological superconductivity, both theoretical and experimental. Various models have been proposed for the realization of TSCs in which MZMs emerge as single excitations at the system's boundaries[16–26]. Furthermore, numerous experiments have been carried out, some of which have reported indirect signatures of MZMs[27–30]. While the search continues, extensive numerical modelling and simulations of TSCs are required in order to speed up the process. The present thesis is part of this effort and is outlined as follows.

In Chapter 2 we provide the theoretical framework on which our simulations are based and discuss details regarding its computational adaption. In Chapter 3 we investigate the connection between our model's effective superconducting coupling parameter and the energy gap, for cubic lattice structures. Then, having chosen a suitable value for the coupling parameter, we model superconducting surfaces and study the effects of single non-magnetic and magnetic impurities embedded in them. After a brief review of the Kitaev model in Chapter 4, we move on to study chains of magnetic impurities embedded in the surface of superconductors. We explore configurations of the magnitude and direction of the impurity atoms' local magnetic fields that can drive such systems in topologically non-trivial phases and identify those phases through the value of a topological invariant: the Majorana number. Having identified the non-collinear magnetic chain as a candidate topological superconductor, in Chapter 5 we focus on that system and further investigate parameters that affect its topological phase, such as the chain's length or the magnetic field's relative angle between adjacent magnetic atoms. Variations of the spin helix model are also studied, by treating the impurities as adatoms on the surface, or by introducing extra layers between the superconductor's surface and the impurity atoms. The thesis is concluded in Chapter 6, where the results obtained through our simulations are summarized and future research paths are proposed.

2 Theoretical Framework

In systems containing a small number of electrons, exact methods can be applied in order to obtain the true many-electron wavefunction. However, in condensed matter physics this is hardly the case, due to the large number of atoms comprising the studied systems. In this case, one of the most eminent methods of dealing with the many-electron problem is the density functional theory (DFT) developed by Hohenberg, Kohn and Sham[31,32], which has the advantage of performing ab-initio electronic structure calculations, without having to calculate the many-electron wavefunction. Despite this method's numerous advantages, its most significant drawback is the large computational time required, even for systems consisting of only a few thousand electrons. For this reason, we shall turn to the tight-binding method, since it allows us to study many-electron systems with a relatively low computational cost and at the same time is more than adequate to provide us with the required physical insight for the problems under study.

2.1 The Tight-Binding Model

Throughout this thesis we shall consider only a single orbital and therefore the usual second quantized tight-binding Hamiltonian describing a system in its normal (i.e. non superconducting) state is written as

$$\check{H}_{\mathrm{N}} = \sum_{\alpha,\alpha',i,j,\sigma,\sigma'} c^{\dagger}_{\alpha i\sigma}\ \check{h}_{\alpha i\sigma,\alpha' j\sigma'}\ c_{\alpha' j\sigma'}\ , \tag{2.1}$$

where

$$\check{h}_{\alpha i\sigma,\alpha' j\sigma'} = \left[-t_{\alpha i,\alpha' j} + (\varepsilon_{\alpha i} - \mu)\,\delta_{\alpha\alpha'}\delta_{ij}\right]\delta_{\sigma\sigma'}\ . \tag{2.2}$$

The indices α, α' correspond to lattice vectors $\mathbf{R}_{\alpha}$ and $\mathbf{R}_{\alpha'}$, respectively, and assume values from 1 to N, where N is the total number of lattice sites. The indices i, j correspond to atom positions $\boldsymbol{\tau}_i$ and $\boldsymbol{\tau}_j$, respectively, in a lattice cell and assume values from 1 to N_b, where N_b is the total number of atoms contained in that cell. As a result, the fermionic operators $c^{\dagger}_{\alpha i\sigma}$ and $c_{\alpha i\sigma}$ create and annihilate, respectively, an electron of spin σ ($\uparrow$ or $\downarrow$) at position $\mathbf{R}_{\alpha} + \boldsymbol{\tau}_i$. The hopping element $t_{\alpha i,\alpha' j}$ satisfies

$$t_{\alpha i,\alpha' j} = t_0 \exp\left(-\frac{\left|\mathbf{R}_\alpha + \boldsymbol{\tau}_i - \mathbf{R}_{\alpha'} - \boldsymbol{\tau}_j\right|}{R_0}\right), \tag{2.3}$$

where R_0 is a constant inserted for dimensional and normalization purposes and t_0 is a tunable parameter. The hopping element is non-zero only as long as $0 \neq \left|\mathbf{R}_\alpha + \boldsymbol{\tau}_i - \mathbf{R}_{\alpha'} - \boldsymbol{\tau}_j\right| < R_{\max}$, where $R_{\max}$ is a cutoff of our choice, allowing us to determine the number of neighbours we wish to be taken into account. As far as the on-site terms are concerned, $\varepsilon_{\alpha i}$ is the self-energy and μ is the system's chemical potential.

Our model's tight-binding Hamiltonian for the normal state,

$$H_{\mathrm{N}} = \sum_{\alpha,\alpha',i,j,\sigma,\sigma'} c^\dagger_{\alpha i\sigma}\ h_{\alpha i\sigma,\alpha' j\sigma'}\ c_{\alpha' j\sigma'}\ , \tag{2.4}$$

incorporates two additional on-site terms, namely

$$h_{\alpha i\sigma,\alpha' j\sigma'} = \check{h}_{\alpha i\sigma,\alpha' j\sigma'} - (\mathbf{B}_{\alpha i}\cdot\boldsymbol{\sigma})_{\sigma\sigma'}\,\delta_{\alpha\alpha'}\delta_{ij} + U_{\alpha i}\,(n_{\alpha i} - \bar{n}_{\alpha i})\,\delta_{\alpha\alpha'}\delta_{ij}\delta_{\sigma\sigma'}\ . \tag{2.5}$$

The first one introduces an effective magnetic field, $\mathbf{B}_{\alpha i}$, which may vary from site to site and atom to atom and gives rise to a local Zeeman energy. Note that, while the Hamiltonian of Eq. (2.1) is block-diagonal because of its symmetricity with respect to the spin indices, this is not the case with the Hamiltonian of Eq. (2.5), due to the dot product between $\mathbf{B}$ and the Pauli vector $\boldsymbol{\sigma} \equiv \left(\boldsymbol{\sigma}_x, \boldsymbol{\sigma}_y, \boldsymbol{\sigma}_z\right)$. As far as the second term is concerned, $n_{\alpha i}$ is the charge density on lattice site α and atom i, $\bar{n}_{\alpha i}$ is the desired value of that charge density and $U_{\alpha i}$ is the so called local charge neutrality (LCN) constant. The purpose of this term is to prevent large charge transfers between atoms by decreasing or increasing their on-site energies, depending on the sign of $(n_{\alpha i} - \bar{n}_{\alpha i})$. It is evident that $U_{\alpha i}$ must be sufficiently large, since, theoretically, the limit $U_{\alpha i} \to \infty$ would yield $n_{\alpha i} = \bar{n}_{\alpha i}$ in order to minimize the ground state's energy.

At this point an important remark must be made. The addition of the local charge neutrality term gives rise to a dependence on the charge densities that the Hamiltonian didn't previously have. However, the densities themselves are calculated from the eigenvectors and eigenvalues of that Hamiltonian, which means that a self-consistency scheme needs to be implemented for the calculations of the system's normal state. As we shall see in Section 2.5, the system's chemical potential can also be determined self-consistently, if we impose specific values for the desired charge densities $\bar{n}_{\alpha i}$, even without turning on the local charge neutrality potential ($U_{\alpha i} = 0$).

2.2 Enter Superconductivity

The Hamiltonian of Eq. (2.4) is only sufficient to describe a system in its non superconducting state, therefore a new term, H_{SC}, must be added to it in order to account for superconducting effects. Following Bogoliubov's[33] generalization of the BCS theory, we may introduce the term

$$H_{\mathrm{SC}} = -\sum_{\alpha,i} \Lambda_{\alpha i} c^{\dagger}_{\alpha i\uparrow} c^{\dagger}_{\alpha i\downarrow} c_{\alpha i\downarrow} c_{\alpha i\uparrow} \ , \tag{2.6}$$

which describes the process of annihilation of two electrons with antiparallel spins (a Cooper pair) and creation of another such pair of electrons. Notice that we have chosen a superconductivity mechanism such that the pairs are annihilated and created on the same site, which is known as on-site or s-wave superconductivity. The minus prefactor has been inserted in order to emphasize the fact that the electron interaction is attractive, as the coupling constant for this process, $\Lambda_{\alpha i}$, is a positive number. In general, $\Lambda_{\alpha i}$ is lattice site- and basis-atom-dependent and within BCS theory it is related to the electron-phonon coupling constant, since conventional superconductivity is mediated by phonons.

The fact that the term introduced in Eq. (2.6) is a two-body operator gives rise to computational difficulties, as our system's Hamiltonian now includes the product of four operators. To tackle this problem, we may perform a Hartree-Fock-like mean-field approximation in order to reduce the two-body operator down to an effective one-body operator and write

$$c_{\alpha i\downarrow} c_{\alpha i\uparrow} = \langle c_{\alpha i\downarrow} c_{\alpha i\uparrow} \rangle - \delta \ , \tag{2.7}$$

where $\delta = \langle c_{\alpha i\downarrow} c_{\alpha i\uparrow} \rangle - c_{\alpha i\downarrow} c_{\alpha i\uparrow}$. The mean-field approximation lies in the assumption that the one-body operator $c_{\alpha i\downarrow} c_{\alpha i\uparrow}$ is close to its mean value and therefore δ is close to the zero operator. This means that terms of $\mathcal{O}\left(\delta^2\right)$ can be ignored. Using Eq. (2.7) we get

$$\begin{aligned} c^{\dagger}_{\alpha i\uparrow} c^{\dagger}_{\alpha i\downarrow} c_{\alpha i\downarrow} c_{\alpha i\uparrow} &= \left|\langle c_{\alpha i\downarrow} c_{\alpha i\uparrow} \rangle\right|^2 - \delta^{\dagger} \langle c_{\alpha i\downarrow} c_{\alpha i\uparrow} \rangle - \langle c^{\dagger}_{\alpha i\uparrow} c^{\dagger}_{\alpha i\downarrow} \rangle \delta + \delta^{\dagger} \delta \\ &\simeq -\left|\langle c_{\alpha i\downarrow} c_{\alpha i\uparrow} \rangle\right|^2 + c^{\dagger}_{\alpha i\uparrow} c^{\dagger}_{\alpha i\downarrow} \langle c_{\alpha i\downarrow} c_{\alpha i\uparrow} \rangle + \langle c^{\dagger}_{\alpha i\uparrow} c^{\dagger}_{\alpha i\downarrow} \rangle c_{\alpha i\downarrow} c_{\alpha i\uparrow} \ , \end{aligned} \tag{2.8}$$

because $\delta^{\dagger}\delta \to 0$ by approximation. The first term of the RHS of Eq. (2.8) can be ignored, for it only contributes as a constant shift to the system's energy without affecting its physical properties, therefore we may define

$$\Delta_{\alpha i} = -\Lambda_{\alpha i} \langle c_{\alpha i\downarrow} c_{\alpha i\uparrow} \rangle = \Lambda_{\alpha i} \langle c_{\alpha i\uparrow} c_{\alpha i\downarrow} \rangle \ , \tag{2.9}$$

where we have used the fact that the fermionic operators obey $c_{\alpha i\downarrow} c_{\alpha i\uparrow} = -c_{\alpha i\uparrow} c_{\alpha i\downarrow}$, and write the mean-field superconductivity Hamiltonian as

$$H_{\mathrm{SC}} \simeq \sum_{\alpha,i} \Delta_{\alpha i} c^{\dagger}_{\alpha i\uparrow} c^{\dagger}_{\alpha i\downarrow} + \Delta^{*}_{\alpha i} c_{\alpha i\downarrow} c_{\alpha i\uparrow} \ . \tag{2.10}$$

The term introduced in Eq. (2.9) is the well known order parameter for superconductivity and is related to the system's superconducting gap and transition temperature.

Combining all the above ingredients, we get the mean-field tight-binding Hamiltonian

$$H_0 = \sum_{\alpha,\alpha',i,j,\sigma,\sigma'} c^{\dagger}_{\alpha i\sigma}\ h_{\alpha i\sigma,\alpha' j\sigma'}\ c_{\alpha' j\sigma'} + \sum_{\alpha,i} \Delta_{\alpha i} c^{\dagger}_{\alpha i\uparrow} c^{\dagger}_{\alpha i\downarrow} + \Delta^{*}_{\alpha i} c_{\alpha i\downarrow} c_{\alpha i\uparrow} \ , \tag{2.11}$$

which is evidently a quadratic form in the electronic operators. After all, this was our end goal when we applied the mean-field approximation.

2.3 Bogoliubov-de Gennes Equations

Given the system's Hamiltonian, the next task is to find its eigenvectors and eigenvalues. It is straightforward to confirm that H_0 satisfies the following commutation relations:

$$\left[c_{\alpha i\uparrow}, H_0\right] = \sum_{\alpha',j,\sigma'} h_{\alpha i\uparrow,\alpha' j\sigma'}\ c_{\alpha' j\sigma'} + \Delta_{\alpha i} c^{\dagger}_{\alpha i\downarrow} \tag{2.12a}$$

$$\left[c^{\dagger}_{\alpha i\uparrow}, H_0\right] = -\sum_{\alpha',j,\sigma'} h_{\alpha' j\sigma',\alpha i\uparrow}\ c^{\dagger}_{\alpha' j\sigma'} - \Delta^{*}_{\alpha i} c_{\alpha i\downarrow} \tag{2.12b}$$

$$\left[c_{\alpha i\downarrow}, H_0\right] = \sum_{\alpha',j,\sigma'} h_{\alpha i\downarrow,\alpha' j\sigma'}\ c_{\alpha' j\sigma'} - \Delta_{\alpha i} c^{\dagger}_{\alpha i\uparrow} \tag{2.12c}$$

$$\left[c^{\dagger}_{\alpha i\downarrow}, H_0\right] = -\sum_{\alpha',j,\sigma'} h_{\alpha' j\sigma',\alpha i\downarrow} c^{\dagger}_{\alpha' j\sigma'} + \Delta^{*}_{\alpha i} c_{\alpha i\uparrow} \tag{2.12d}$$

In these relations the electron creation operators are coupled not only between themselves, but also with electron annihilation operators and vice versa, due to the superconductivity coupling. This illuminates the fact that in order to diagonalize the Hamiltonian, one needs to express the electronic operators as linear combinations of electron- and hole-like quasiparticle excitations. For this purpose we apply the canonical transformation

$$c_{\alpha i\uparrow} = \sum_{n}{}' u^{n}_{\alpha i\uparrow}\gamma_n - v^{n*}_{\alpha i\uparrow}\gamma^{\dagger}_n, \qquad c_{\alpha i\downarrow} = \sum_{n}{}' u^{n}_{\alpha i\downarrow}\gamma_n + v^{n*}_{\alpha i\downarrow}\gamma^{\dagger}_n. \tag{2.13}$$

Here, $\gamma^{\dagger}_n$ and γ_n are quasiparticle creation and annihilation operators, respectively, and n labels a complete set of states, also incorporating the quasiparticles' pseudo-spin index. The fact that the operators which appear in the LHS of the transformation (2.13) are fermionic enforces that the quasiparticle operators also obey the usual anti-commutation relations. The u^n and v^n coefficients correspond to the electron- and hole-like parts of the quasiparticles,

respectively, and are directly related to the Hamiltonian's eigenvectors. A subtle but very important point that has to be emphasized is the fact that the summations in the canonical transformation extend only over values of n for which the corresponding eigenvalues (energies) are positive, hence the prime sign above the summation symbols. The reason why this is essential will be clarified shortly.

Since the introduction of the canonical transformation was made in order to diagonalize the system's Hamiltonian, Eq. (2.11) can be expressed in the form

$$H_0 = E_{\text{gs}} + \sum_n \epsilon_n \gamma_n^\dagger \gamma_n, \tag{2.14}$$

where E_{gs} is a constant term equal to the system's ground state energy, while ϵ_n are the energies corresponding to the quasiparticle excited states. Using this form of the Hamiltonian, it becomes evident that

$$[H_0, \gamma_n] = -\epsilon_n \gamma_n \quad \text{and} \quad \left[H_0, \gamma_n^\dagger\right] = \epsilon_n \gamma_n^\dagger. \tag{2.15}$$

This fixes the coefficients u^n and v^n in the canonical transformation and the equations for them can be derived by substitution of Eq. (2.13) into Eqs. (2.12) and subsequent substitution of Eq. (2.15) in the LHS of Eqs. (2.12). Comparing the coefficients of the terms with γ_n and $\gamma_n^\dagger$ yields

$$\epsilon_n u^n_{\alpha i\uparrow} = \sum_{\alpha',j,\sigma'}{}' h_{\alpha i\uparrow,\alpha' j\sigma'}\, u^n_{\alpha' j\sigma'} + \Delta_{\alpha i} v^n_{\alpha i\downarrow}\,, \tag{2.16a}$$

$$\epsilon_n u^n_{\alpha i\downarrow} = \sum_{\alpha',j,\sigma'}{}' h_{\alpha i\downarrow,\alpha' j\sigma'}\, u^n_{\alpha' j\sigma'} + \Delta_{\alpha i} v^n_{\alpha i\uparrow}\,, \tag{2.16b}$$

$$\epsilon_n v^n_{\alpha i\uparrow} = -\sum_{\alpha',j}{}' h^*_{\alpha i\uparrow,\alpha' j\uparrow}\, v^n_{\alpha' j\uparrow} + \sum_{\alpha',j}{}' h^*_{\alpha i\uparrow,\alpha' j\downarrow}\, v^n_{\alpha' j\downarrow} + \Delta^*_{\alpha i} u^n_{\alpha i\downarrow}\,, \tag{2.16c}$$

$$\epsilon_n v^n_{\alpha i\downarrow} = \sum_{\alpha',j}{}' h^*_{\alpha i\downarrow,\alpha' j\uparrow}\, v^n_{\alpha' j\uparrow} - \sum_{\alpha',j}{}' h^*_{\alpha i\downarrow,\alpha' j\downarrow}\, v^n_{\alpha' j\downarrow} + \Delta^*_{\alpha i} u_{\alpha i\uparrow}\,. \tag{2.16d}$$

These are known as the Bogoliubov-de Gennes[34] (BdG) equations. Notice that the electron-like u^n coefficients are coupled not only between themselves, but also with the hole-like coefficients v^n, a result consistent with the fact that the electron creation operators were also coupled with the electron annihilation operators in Eqs. (2.12). If one defines the four-component spinor $\mathbf{\Psi}^n_{\alpha i}$ as

$$\mathbf{\Psi}^n_{\alpha i} \coloneqq \left(u^n_{\alpha i\uparrow}\; u^n_{\alpha i\downarrow}\; v^n_{\alpha i\uparrow}\; v^n_{\alpha i\downarrow}\right)^{\mathrm{T}}, \tag{2.17}$$

then the BdG equations can be cast into matrix form as

$$\sum_{\alpha',j} \boldsymbol{\mathcal{H}}^0_{\alpha i,\alpha' j} \cdot \boldsymbol{\Psi}^n_{\alpha' j} = \epsilon_n \boldsymbol{\Psi}^n_{\alpha i}, \tag{2.18}$$

where

$$\boldsymbol{\mathcal{H}}^0_{\alpha i,\alpha' j} = \begin{pmatrix} h_{\alpha i\uparrow,\alpha' j\uparrow} & h_{\alpha i\uparrow,\alpha' j\downarrow} & 0 & \Delta_{\alpha i}\delta_{\alpha\alpha'}\delta_{ij} \\ h_{\alpha i\downarrow,\alpha' j\uparrow} & h_{\alpha i\downarrow,\alpha' j\downarrow} & \Delta_{\alpha i}\delta_{\alpha\alpha'}\delta_{ij} & 0 \\ 0 & \Delta^*_{\alpha i}\delta_{\alpha\alpha'}\delta_{ij} & -h^*_{\alpha i\uparrow,\alpha' j\uparrow} & h^*_{\alpha i\uparrow,\alpha' j\downarrow} \\ \Delta^*_{\alpha i}\delta_{\alpha\alpha'}\delta_{ij} & 0 & h^*_{\alpha i\downarrow,\alpha' j\uparrow} & -h^*_{\alpha i\downarrow,\alpha' j\downarrow} \end{pmatrix} \tag{2.19}$$

is a matrix element of the so called BdG Hamiltonian[1], $\boldsymbol{\mathcal{H}}^0$. The BdG Hamiltonian is the $4N_bN \times 4N_bN$ matrix whose eigenvectors are the $4N_bN$-component spinors

$$\boldsymbol{\Psi}^n = \left(\boldsymbol{u}^n_\uparrow \; \boldsymbol{u}^n_\downarrow \; \boldsymbol{v}^n_\uparrow \; \boldsymbol{v}^n_\downarrow\right)^{\mathrm{T}}, \tag{2.20}$$

where $\boldsymbol{u}^n_\sigma$ and $\boldsymbol{v}^n_\sigma$ are N_bN-dimensional vectors containing the BdG equations' solutions for every lattice site and basis-atom. The BdG Hamiltonian can be interpreted as the first quantization Hamiltonian that governs the quasiparticles' dynamics via

$$\boldsymbol{\mathcal{H}}^0 \cdot \boldsymbol{\Psi}^n(t) = \mathrm{i}\hbar \frac{\partial}{\partial t} \boldsymbol{\Psi}^n(t), \tag{2.21}$$

since the elements of the spinor in Eq. (2.20) are not field operators, but wavefunctions. The problem of diagonalizing the BdG Hamiltonian is equivalent to solving the BdG equations, which in turn is equivalent to determining the spectrum of eigenvectors and eigenvalues of the system's Hamiltonian, H_0, because of the canonical transformation of Eq. (2.13).

Let us now return to that canonical transformation and explain why the summations extend only over values of n which correspond to positive energies. In practice, that transformation enforces what is known as particle-hole (or charge conjugation) symmetry (PHS) to the studied system, which is a fundamental property of every mean-field theory of superconductivity[2]. Effectively, this leads to a doubling of the system's degrees of freedom, since the creation/annihilation of a hole is equivalent to the annihilation/creation of an electron. The spinor of Eq. (2.17) is a four-component spinor due to the distinction between $\uparrow$ and $\downarrow$

[1] The reason why the 34 and 43 matrix elements in Eq. (2.19) do not carry negative signs, as is more common in literature, is due to our choice of a negative sign for the $v^{n*}_{\alpha i\uparrow}$ coefficient in the canonical transformation of Eq. (2.13).

[2] The term particle-hole symmetry is often used in general to describe systems whose energy spectra and their corresponding spectral densities are symmetric around zero. In our case, the term corresponds to the symmetry (2.23), which arises because we artificially doubled the system's degrees of freedom, thus ensuring that all energies E come in pairs $\{E, -E\}$.

as far as spin is concerned, as well as the distinction between u and v, as far as particles and holes are concerned. Let us define the operator $\mathcal{P}$, such that

$$\mathcal{P} \coloneqq -\boldsymbol{\sigma}_{\mathrm{z}} \otimes \boldsymbol{\tau}_{\mathrm{x}} \mathcal{K}, \tag{2.22}$$

where $\boldsymbol{\sigma}_{\mathrm{z}}$ is the z Pauli matrix, which acts on the spin components of a matrix or vector, $\boldsymbol{\tau}_{\mathrm{x}}$ is the x Pauli matrix, which acts on the particle/hole components of a matrix or vector, the symbol $\otimes$ denotes the tensor product between them and $\mathcal{K}$ is the complex conjugation operator. This operator satisfies

$$\mathcal{P} \boldsymbol{\mathcal{H}}^0_{\alpha i, \alpha' j} \mathcal{P}^{-1} = -\boldsymbol{\mathcal{H}}^0_{\alpha i, \alpha' j}, \tag{2.23}$$

which indicates that if $\boldsymbol{\Psi}^n = \left(\boldsymbol{u}^n_{\uparrow}\ \boldsymbol{u}^n_{\downarrow}\ \boldsymbol{v}^n_{\uparrow}\ \boldsymbol{v}^n_{\downarrow}\right)^{\mathrm{T}}$ is an eigenvector of $\boldsymbol{\mathcal{H}}^0$ with eigenvalue ϵ_n, then $\mathcal{P}\boldsymbol{\Psi}^n = \left(-\boldsymbol{v}^{n*}_{\uparrow}\ \boldsymbol{v}^{n*}_{\downarrow} - \boldsymbol{u}^{n*}_{\uparrow}\ \boldsymbol{u}^{n*}_{\downarrow}\right)^{\mathrm{T}}$ will also be an eigenvector of $\boldsymbol{\mathcal{H}}^0$, with eigenvalue $-\epsilon_n$. This result shows that $\mathcal{P}$ is in fact the PHS operator[3] and illustrates that the solutions of the BdG equations come in pairs. As a consequence, summing over values of n which correspond to positive energies in Eq. (2.13) in a sense ensures that we avoid double counting. This symmetry will prove to be quite useful in simplifying some of the calculations that involve the solutions of the BdG equations.

2.3.1 Self-Consistency

The concept of self-consistency was first introduced while discussing the normal state Hamiltonian of Eq. (2.4), where the charge densities appeared as terms of the Hamiltonian, however couldn't be determined without that Hamiltonian's eigenvectors and eigenvalues. The way this problem is tackled is by making an initial guess for the densities, diagonalizing the Hamiltonian and then calculating them anew. The calculated charge densities are then inserted into the Hamiltonian, which is again diagonalized and produces new ones. This process is repeated until the charge densities that are inserted into the Hamiltonian are identical[4] to those that are calculated after the diagonalization. This is known as a self-consistency scheme and it also needs to be applied for the solutions of the BdG equations. The charge density per spin $n_{\alpha i \sigma}$ of a basis-atom i with spin σ on lattice site α is simply the mean value of the number operator,

$$n_{\alpha i \sigma} = \langle c^{\dagger}_{\alpha i \sigma} c_{\alpha i \sigma} \rangle. \tag{2.24}$$

---

[3] Note that the PHS operator depends on our choice of basis, so the expression of Eq. (2.22) corresponds to a PHS operator only in the basis that is defined by Eq. (2.17).

[4] In practice, the "input" and "output" charges will never be exactly equal. As we shall see in Section 2.5, the self-consistency scheme is terminated once the difference between the input and output charges crosses a threshold of our choice.

Substituting the canonical transformation (2.13) in this equation allows us to express the charge density per spin in terms of the γ_n and $\gamma_n^\dagger$ operators. Since the mean value is evaluated for a Hamiltonian's eigenstate, and taking into account the fact that the quasiparticles are non-interacting,

$$\langle \gamma_n \gamma_m \rangle = 0 = \langle \gamma_n^\dagger \gamma_m^\dagger \rangle \quad \text{and} \quad \langle \gamma_n^\dagger \gamma_m \rangle = \delta_{nm} f(\epsilon_n) \tag{2.25}$$

must hold, where

$$f(\epsilon_n) = \frac{1}{\exp\left(\epsilon_n / k_{\mathrm{B}} T\right) + 1} \tag{2.26}$$

is the Fermi function at temperature T. Notice that the chemical potential in the Fermi function is set to zero, since it corresponds to quasiparticles, the number of which is not a conserved quantity[(5)]. Using Eqs. (2.25) leads to

$$n_{\alpha i\sigma} = {\sum_n}' |u^n_{\alpha i\sigma}|^2 f(\epsilon_n) + |v^n_{\alpha i\sigma}|^2 f(-\epsilon_n). \tag{2.27}$$

By extending the summation over all energies, one may only keep the first term of this expression, since PHS dictates that $|v^n_{\alpha i\sigma}|^2 f(-\epsilon_n)$ is equivalent to $|u^n_{\alpha i\sigma}|^2 f(\epsilon_n)$. The self-consistency condition for the charge densities is therefore simplified to

$$n_{\alpha i} = \sum_{n,\sigma} |u^n_{\alpha i\sigma}|^2 f(\epsilon_n). \tag{2.28}$$

However, the charge densities are not the only physical quantities that need to be calculated self-consistently. Returning to the definition of the order parameter in Eq. (2.9) it becomes evident that it also is dependent on the BdG equations' solutions, due to the term

$$\chi_{\alpha i} = \langle c_{\alpha i\uparrow} c_{\alpha i\downarrow} \rangle, \tag{2.29}$$

which is usually called the anomalous density. Following the same procedure, the anomalous density can be written as

$$\chi_{\alpha i} = {\sum_n}' u^n_{\alpha i\uparrow} v^{n*}_{\alpha i\downarrow} f(-\epsilon_n) - u^n_{\alpha i\downarrow} v^{n*}_{\alpha i\uparrow} f(\epsilon_n) \tag{2.30}$$

and taking into account the PHS this expression is further simplified to

$$\chi_{\alpha i} = -\sum_n u^n_{\alpha i\downarrow} v^{n*}_{\alpha i\uparrow} f(\epsilon_n). \tag{2.31}$$

[(5)] The number N_{ex} of such excitations is not constant, and is therefore a variable which needs to minimize the system's free energy $\mathcal{F}$, i.e. $\partial\mathcal{F}/\partial N_{\mathrm{ex}} = 0$ must hold. However, this derivative is none other but the quasiparticles' chemical potential.

2.3.2 Bloch's Theorem

So far, no assumptions have been made as far as the lattice is concerned. If we now assume that the parameters entering the system's Hamiltonian[6] are not lattice site-dependent but only basis-atom-dependent, then they can be easily expressed as trivial summations over their corresponding densities. We may therefore write, for example,

$$\Delta_i = \Lambda_i \chi_{\alpha i} \quad \text{and} \quad n_i = n_{\alpha i}. \tag{2.32}$$

From a computational standpoint, solving the BdG equations is equivalent to the diagonalization of the $4N_b N \times 4N_b N$ matrix $\boldsymbol{\mathcal{H}}^0$. However, if all the aforementioned parameters are only basis-atom-dependent, we may consider setting up the system on periodic lattices. In this case, Bloch's theorem allows us to greatly simplify the process of solving the BdG equations: the BdG Hamiltonian is block-diagonal in reciprocal space, therefore the problem is simplified to the diagonalization of N matrices with dimension $4N_b \times 4N_b$. For this purpose, we may define a new basis by introducing the four-component spinor $\boldsymbol{\Phi}_i^n(\mathbf{k})$, where $\mathbf{k}$ corresponds to a Bloch wavevector, as

$$\boldsymbol{\Phi}_i^n(\mathbf{k}) \coloneqq \frac{1}{\sqrt{N}} \sum_{\alpha} e^{-\mathrm{i}\mathbf{k}\cdot\left(\mathbf{R}_\alpha + \boldsymbol{\tau}_i\right)} \boldsymbol{\Psi}_{\alpha i}^n. \tag{2.33}$$

This is essentially the Fourier transform of $\boldsymbol{\Psi}_{\alpha i}^n$, while the inverse transform is simply

$$\boldsymbol{\Psi}_{\alpha i}^n = \frac{1}{\sqrt{N}} \sum_{\mathbf{k}} e^{\mathrm{i}\mathbf{k}\cdot\left(\mathbf{R}_\alpha + \boldsymbol{\tau}_i\right)} \boldsymbol{\Phi}_i^n(\mathbf{k}). \tag{2.34}$$

The BdG equations can now be written as

$$\sum_j \widetilde{\boldsymbol{\mathcal{H}}}_{i,j}^0(\mathbf{k}) \cdot \boldsymbol{\Phi}_j^n(\mathbf{k}) = \epsilon_n(\mathbf{k})\, \boldsymbol{\Phi}_i^n(\mathbf{k}), \tag{2.35}$$

for every $\mathbf{k}$, where

$$\widetilde{\boldsymbol{\mathcal{H}}}_{i,j}^0(\mathbf{k}) = \sum_{\xi} \boldsymbol{\mathcal{H}}_{0i,\xi j}^0 \; e^{i\mathbf{k}\cdot\left(\mathbf{R}_\xi + \boldsymbol{\tau}_j - \boldsymbol{\tau}_i\right)}. \tag{2.36}$$

Note that the index n labels the sets of the BdG equations' solutions. This means that, while in Eq. (2.18) n assumed values $n = 1, 2, \ldots, 4N_b N$, in Eq. (2.36) it assumes values $n = 1, 2, \ldots, 4N_b$, since it is $\mathbf{k}$-dependent in reciprocal space. The charge and anomalous densities are written as

$$n_i(\mathbf{k}) = \sum_{n,\sigma} |u_{i\sigma}^n(\mathbf{k})|^2 f(\epsilon_n) \tag{2.37}$$

[6] Specifically, the self-energies, the local magnetic fields, the local charge neutrality constants, the charges, the superconductivity coupling constants and the order parameters.

and

$$\chi_i(\mathbf{k}) = -\sum_n u^n_{i\downarrow}(\mathbf{k})\, v^{n*}_{i\uparrow}(\mathbf{k})\, f(\epsilon_n), \tag{2.38}$$

respectively. As a result, the self-consistency condition for the charges is

$$n_i = \frac{1}{N}\sum_{\mathbf{k}} n_i(\mathbf{k}) = \frac{1}{N}\sum_{\mathbf{k},n,\sigma} |u^n_{i\sigma}(\mathbf{k})|^2 f(\epsilon_n), \tag{2.39}$$

while the self-consistency condition for the order parameters is

$$\Delta_i = \frac{\Lambda_i}{N}\sum_{\mathbf{k}} \chi_i(\mathbf{k}) = -\frac{\Lambda_i}{N}\sum_{\mathbf{k},n} u^n_{i\downarrow}(\mathbf{k})\, v^{n*}_{i\uparrow}(\mathbf{k})\, f(\epsilon_n). \tag{2.40}$$

2.4 The Impurity Problem

The drawback of studying periodic systems is the fact that the introduction of interfaces or impurities destroys the lattice periodicity and therefore the Bloch wavevector stops being a good quantum number. Specifically in the case of impurities, in order to study their effects one has to redefine the system's Hamiltonian as

$$H = H_0 + \delta H, \tag{2.41}$$

where H_0 corresponds to the unperturbed periodic system, known as the "host" system, while δH corresponds to the changes induced by the impurities. Then, the Green function method is applied in order to determine how physical quantities such as the charges or the order parameter are affected by these perturbations, without having to calculate the eigenvectors and eigenvalues of the full Hamiltonian, H.

In the context of the BdG formalism, the superconducting host system corresponds to the BdG Hamiltonian with matrix elements given by Eq. (2.19). Using the solutions of the BdG equations (2.35), the Green function can be calculated for the host system in reciprocal space as

$$\widetilde{\boldsymbol{\mathcal{G}}}^0_{i,j}(\mathbf{k}; z) = \sum_n \frac{\boldsymbol{\Phi}^n_i(\mathbf{k}) \cdot \boldsymbol{\Phi}^{n\dagger}_j(\mathbf{k})}{z - \epsilon_n(\mathbf{k})}. \tag{2.42}$$

This is the spectral representation of the Green function, which can be used because, due to the mean-field treatment of superconductivity, the BdG Hamiltonian describes a single-particle problem. Performing the inverse Fourier transform of Eq. (2.42) and taking into account the lattice's periodicity yields

$$\boldsymbol{\mathcal{G}}^0_{i,j}(\mathbf{R}_\xi; z) = \frac{1}{N}\sum_{\mathbf{k}} \widetilde{\boldsymbol{\mathcal{G}}}^0_{i,j}(\mathbf{k}; z)\, e^{-\mathrm{i}\mathbf{k}\cdot(\mathbf{R}_\xi + \boldsymbol{\tau}_j - \boldsymbol{\tau}_i)}\ , \tag{2.43}$$

which is the Green function for the host system in configuration space. An interesting feature of the Green function is that it allows for the calculation of the local density of states (LDoS) $\mathcal{D}_{\xi i}(\epsilon)$ for an atom i on lattice site ξ as

$$\mathcal{D}_{\xi i}(\epsilon) = -\frac{1}{\pi}\lim_{\eta\to 0^+}\mathrm{Im}\left[\mathcal{G}^0_{i,i}\left(\mathbf{R}_\xi; z\right)_{11} + \mathcal{G}^0_{i,i}\left(\mathbf{R}_\xi; z\right)_{22}\right], \tag{2.44}$$

where we have taken $z = \epsilon + \mathrm{i}\eta$, which is equivalent to using the retarded Green function, and the new numeric indices correspond to the Green function's matrix elements[7].

The impurities introduced on the superconducting host system will be described by a $\delta\boldsymbol{\mathcal{H}}$ matrix, the elements of which assume the form

$$\delta\boldsymbol{\mathcal{H}}_{\alpha i,\alpha' j} = \begin{pmatrix} \delta h_{\alpha i\uparrow,\alpha' j\uparrow} & \delta h_{\alpha i\uparrow,\alpha' j\downarrow} & 0 & \delta\Delta_{\alpha i}\delta_{\alpha\alpha'}\delta_{ij} \\ \delta h_{\alpha i\downarrow,\alpha' j\uparrow} & \delta h_{\alpha i\downarrow,\alpha' j\downarrow} & \delta\Delta_{\alpha i}\delta_{\alpha\alpha'}\delta_{ij} & 0 \\ 0 & \delta\Delta^*_{\alpha i}\delta_{\alpha\alpha'}\delta_{ij} & -\delta h^*_{\alpha i\uparrow,\alpha' j\uparrow} & \delta h^*_{\alpha i\uparrow,\alpha' j\downarrow} \\ \delta\Delta^*_{\alpha i}\delta_{\alpha\alpha'}\delta_{ij} & 0 & \delta h^*_{\alpha i\downarrow,\alpha' j\uparrow} & -\delta h^*_{\alpha i\downarrow,\alpha' j\downarrow} \end{pmatrix} \tag{2.45}$$

in configuration space, where α, α' and i, j are lattice site and atom indices, respectively, now corresponding to substitutional impurities' coordinates. Furthermore,

$$\begin{aligned}\delta h_{\alpha i\sigma,\alpha' j\sigma'} = &\left[\varepsilon^{\mathrm{imp}}_{\alpha i} - \varepsilon_{\alpha i} + U^{\mathrm{imp}}_{\alpha i}\left(n^{\mathrm{imp}}_{\alpha i} - \bar{n}^{\mathrm{imp}}_{\alpha i}\right) - U_{\alpha i}\left(n_{\alpha i} - \bar{n}_{\alpha i}\right)\right]\delta_{\alpha\alpha'}\delta_{ij}\delta_{\sigma\sigma'} - \\ &- \left[\left(\mathbf{B}^{\mathrm{imp}}_{\alpha i} - \mathbf{B}_{\alpha i}\right)\cdot\boldsymbol{\sigma}\right]_{\sigma\sigma'}\delta_{\alpha\alpha'}\delta_{ij}\end{aligned} \tag{2.46}$$

and

$$\delta\Delta_{\alpha i} = \Lambda^{\mathrm{imp}}_{\alpha i}\chi^{\mathrm{imp}}_{\alpha i} - \Lambda_{\alpha i}\chi_{\alpha i}\ , \tag{2.47}$$

where the parameters carrying the "imp" index describe the impurities that substituted the host system's atoms. The full system's - including the impurities - Green function, $\boldsymbol{\mathcal{G}}$, is given by Dyson's equation

$$\boldsymbol{\mathcal{G}} = \boldsymbol{\mathcal{G}}^0 + \boldsymbol{\mathcal{G}}^0\cdot\delta\boldsymbol{\mathcal{H}}\cdot\boldsymbol{\mathcal{G}}, \tag{2.48}$$

or, equivalently,

$$\boldsymbol{\mathcal{G}} = \left(\mathbf{I} - \boldsymbol{\mathcal{G}}^0\cdot\delta\boldsymbol{\mathcal{H}}\right)^{-1}\cdot\boldsymbol{\mathcal{G}}^0. \tag{2.49}$$

[7] In this case, taking the trace over all of the Green function's diagonal elements would result into LDoS diagrams on which the built-in PHS symmetry of the BdG formalism would be engraved: the spectral densities for each energy would be symmetric around zero. While this choice is more common in literature, we opt to only sum over the Green function's particle-like components, i.e. the 11 and 22 elements, in order to have access to the diagram's full information. The particle-hole symmetric LDoS diagram can be acquired simply by mirroring the diagram obtained via Eq. (2.44) around zero.

After solving Dyson's equation, the full system's Green function can be utilized in order to calculate the charge and anomalous densities. Choosing $z = \epsilon + \mathrm{i}\eta$, the charge density for each spin flavour is

$$n_{\xi i\uparrow/\downarrow} = -\frac{1}{\pi} \lim_{\eta\to 0^+} \int_{-\infty}^{\infty} d\epsilon \ \mathrm{Im}\left[f(z)\, \mathcal{G}_{i,i}\left(\mathbf{R}_\xi; z\right)_{11/22} \right] \tag{2.50}$$

and the anomalous density is

$$\chi_{\xi i} = \frac{1}{\pi} \lim_{\eta\to 0^+} \int_{-\infty}^{\infty} d\epsilon \ \mathrm{Im}\left[f(z)\, \mathcal{G}_{i,i}\left(\mathbf{R}_\xi; z\right)_{23} \right]. \tag{2.51}$$

Since the solution of Dyson's equation allows us to calculate the charges and order parameters using Eqs. (2.50) and (2.51), but also requires them as inputs, it becomes evident that, once again, this process has to be performed in a self-consistent manner.

2.5 Computational Adaptation

In our code, the BdG equations for the host system are solved in reciprocal space. The $4N_b$-component spinor

$$\boldsymbol{\Phi}^n(\mathbf{k}) = \left(\boldsymbol{u}^n_\uparrow(\mathbf{k}) \ \ \boldsymbol{u}^n_\downarrow(\mathbf{k}) \ \ \boldsymbol{v}^n_\uparrow(\mathbf{k}) \ \ \boldsymbol{v}^n_\downarrow(\mathbf{k}) \right)^{\mathrm{T}}, \tag{2.52}$$

where

$$\boldsymbol{u}^n_\sigma(\mathbf{k}) = \left(u^n_{1\sigma}(\mathbf{k}) \ \ u^n_{2\sigma}(\mathbf{k}) \ \ \cdots \ \ u^n_{N_b\sigma}(\mathbf{k}) \right)^{\mathrm{T}}, \tag{2.53a}$$

$$\boldsymbol{v}^n_\sigma(\mathbf{k}) = \left(v^n_{1\sigma}(\mathbf{k}) \ \ v^n_{2\sigma}(\mathbf{k}) \ \ \cdots \ \ v^n_{N_b\sigma}(\mathbf{k}) \right)^{\mathrm{T}}, \tag{2.53b}$$

incorporates the four-component spinors of all atoms in the unit cell. The BdG Hamiltonian per $\mathbf{k}$ is a $4N_b \times 4N_b$ matrix which is constructed as

$$\widetilde{\boldsymbol{\mathcal{H}}}^0(\mathbf{k}) = \begin{pmatrix} \boldsymbol{h}_{\uparrow\uparrow}(\mathbf{k}) & \boldsymbol{h}_{\uparrow\downarrow}(\mathbf{k}) & 0 & \boldsymbol{\Delta} \\ \boldsymbol{h}_{\downarrow\uparrow}(\mathbf{k}) & \boldsymbol{h}_{\downarrow\downarrow}(\mathbf{k}) & \boldsymbol{\Delta} & 0 \\ 0 & \boldsymbol{\Delta}^* & -\boldsymbol{h}^*_{\uparrow\uparrow}(\mathbf{k}) & \boldsymbol{h}^*_{\uparrow\downarrow}(\mathbf{k}) \\ \boldsymbol{\Delta}^* & 0 & \boldsymbol{h}^*_{\downarrow\uparrow}(\mathbf{k}) & -\boldsymbol{h}^*_{\downarrow\downarrow}(\mathbf{k}) \end{pmatrix}, \tag{2.54}$$

where

$$\boldsymbol{\Delta} = \mathrm{diag}\left(\Delta_1 \ \Delta_2 \ \cdots \ \Delta_{N_b} \right) \tag{2.55}$$

and

$$\boldsymbol{h}_{\sigma\sigma'}(\mathbf{k}) = \begin{pmatrix} h_{1\sigma,1\sigma'}(\mathbf{k}) & h_{1\sigma,2\sigma'}(\mathbf{k}) & \dots & h_{1\sigma,N_b\sigma'}(\mathbf{k}) \\ h_{2\sigma,1\sigma'}(\mathbf{k}) & h_{2\sigma,2\sigma'}(\mathbf{k}) & \dots & h_{1\sigma,N_b\sigma'}(\mathbf{k}) \\ \vdots & \vdots & \ddots & \vdots \\ h_{N_b\sigma,1\sigma'}(\mathbf{k}) & h_{N_b\sigma,2\sigma'}(\mathbf{k}) & \dots & h_{N_b\sigma,N_b\sigma'}(\mathbf{k}) \end{pmatrix}. \tag{2.56}$$

The matrix elements of $\boldsymbol{h}_{\sigma\sigma'}(\mathbf{k})$ are calculated as indicated by the Fourier transform (2.36). The BdG equations per $\mathbf{k}$ are therefore written as

$$\widetilde{\boldsymbol{\mathcal{H}}}^0(\mathbf{k}) \cdot \boldsymbol{\Phi}^n(\mathbf{k}) = \epsilon_n \boldsymbol{\Phi}^n(\mathbf{k}) \tag{2.57}$$

and the full Hamiltonian in reciprocal space is

$$\widetilde{\boldsymbol{\mathcal{H}}}^0 = \bigoplus_{\mathbf{k}} \widetilde{\boldsymbol{\mathcal{H}}}^0(\mathbf{k}). \tag{2.58}$$

The computational process leading to the solution of the impurity problem is summarized in the flowchart of Fig. 2.1. First, the BdG equations are solved self-consistently for the host system's normal state and the solutions are used in order to calculate the chemical potential, as well as the atomic charges. Note that in this case the BdG Hamiltonian per $\mathbf{k}$ (2.54) is block-diagonal, since the normal state corresponds to $\Delta_i = 0$, for every atom i. As a result, the problem is reduced to the diagonalization of the upper $2N_b \times 2N_b$ block. If, in addition, $\mathbf{B}_i = \mathbf{0}$, for all atoms i, then $\boldsymbol{h}_{\uparrow\downarrow}(\mathbf{k}) = 0 = \boldsymbol{h}_{\downarrow\uparrow}(\mathbf{k})$ and $\boldsymbol{h}_{\uparrow\uparrow}(\mathbf{k}) = \boldsymbol{h}_{\downarrow\downarrow}(\mathbf{k})$, so the problem is further reduced to the diagonalization of $\boldsymbol{h}_{\uparrow\uparrow}(\mathbf{k})$. Using the calculated charges as initial values and keeping the chemical potential constant, another self-consistency cycle is initiated in order to calculate the host system's properties for the superconducting state. Once convergence is achieved for the charges and the order parameters, the host's Green function is calculated using the eigenvectors and eigenvalues of Eq. (2.57) and then Fourier transformed to configuration space. Finally, after introducing impurities into the host system, Dyson's equation is solved self-consistently, yielding the full system's Green function, which can be used to calculate the charge and anomalous density at any lattice site.

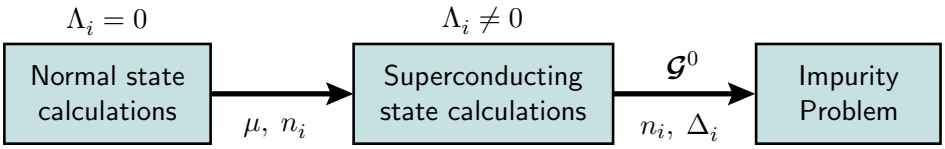

Figure 2.1: Flowchart of the computational solution of the BdG Equations and the impurity problem.

Details about the three self-consistency schemes mentioned and their corresponding convergence criteria can be found in Appendix A.1.

2.5.1 Parameters and Units

For all simulations performed throughout this thesis, Boltzmann's constant is assumed to be $k_{\mathrm{B}} = 1$, therefore all temperatures are measured in units of energy. In addition, all energy parameters are normalized to the value of the hopping element (2.3), e.g. $B \mapsto B/t$. As far as the hopping element is concerned, R_{max} is chosen such, that only nearest-neighbour hopping is considered for all simulations. All lattice distances are measured in terms of the lattice constant and R_0 in Eq. (2.3) is taken equal to 1. Finally, the order parameter is assumed to be real.

3 Impurities Embedded in Superconductor Surfaces

3.1 Effective Coupling Constant

The effective coupling constant, Λ, introduced in Bogoliubov's theory is the key parameter in the study of superconducting materials, since non-zero values thereof lead to the formation of the gap, provided that the temperature is low enough. Within the context of BCS superconductivity, Λ is the analogue to V, the coupling strength of the electron-electron attractive interaction mediated by the lattice phonons. Its relation to the order parameter, Δ, at zero temperature in the weak-coupling limit is given by [35]

$$\Delta = 2\hbar\omega_{\mathrm{D}} \exp\left[-\frac{1}{V\mathcal{D}\left(E_{\mathrm{F}}\right)}\right], \tag{3.1}$$

where $\hbar\omega_{\mathrm{D}}$ is the Debye energy and $\mathcal{D}\left(E_{\mathrm{F}}\right)$ is the system's density of states per spin at the Fermi energy for its normal state. Studying gap properties or the formation of in-gap states (for example due to the presence of impurities) is easier if the system's gap is sufficiently large. We therefore begin by investigating the resulting order parameter for several values of the coupling constant, in order to gain some insight regarding the proper choice of Λ for the simulations performed throughout this thesis. To this end, we solve the BdG equations self-consistently for $0.0 \leq \Lambda \leq 3.0$ in the case of homogenous 3-dimensional superconductors with simple cubic (SC), base centered cubic (BCC) and face centered cubic (FCC) structures. The temperature is set to zero, while the values for the rest of the parameters are $\varepsilon = 0.0$ and $\bar{n} = 1.0$. The resulting diagram can be seen in Fig. 3.1, where the solid, dashed and dotted lines correspond to the SC, BCC and FCC structures, respectively.

It is evident that the order parameters satisfy $\Delta_{\mathrm{BCC}} > \Delta_{\mathrm{SC}} > \Delta_{\mathrm{FCC}}$ for all values of the coupling constant. Our choice of $\bar{n} = 1.0$ corresponds to half-filling (exactly one electron per site) and the converged values for the spectral densities per spin at the Fermi level in the normal state are $\mathcal{D}_{\mathrm{SC}}\left(E_{\mathrm{F}}\right) = 0.294$, $\mathcal{D}_{\mathrm{BCC}}\left(E_{\mathrm{F}}\right) = 0.891$ and $\mathcal{D}_{\mathrm{FCC}}\left(E_{\mathrm{F}}\right) = 0.259$. This means that, even though our model is not equivalent to BCS theory, these results are consistent with Eq. (3.1), which indicates that larger values of $\mathcal{D}\left(E_{\mathrm{F}}\right)$ lead to larger values of Δ. Furthermore, in all three cases, non-zero values of Λ always induce a gap, however the

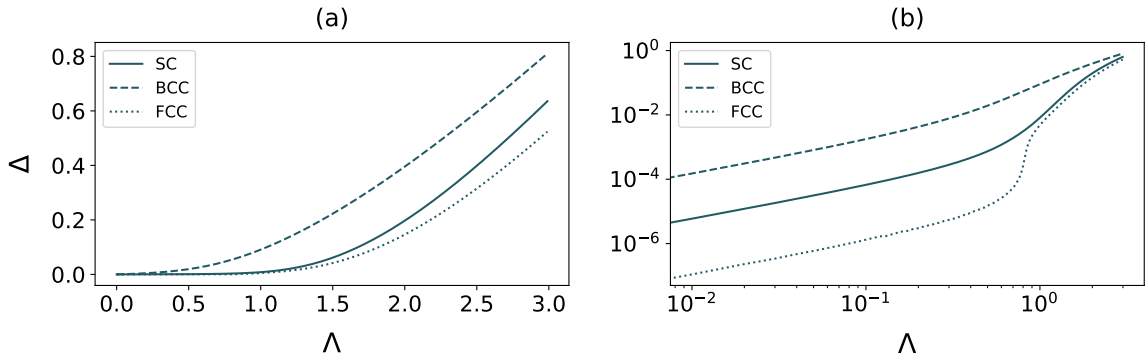

Figure 3.1: The induced superconducting gap Δ for each value of the coupling constant Λ, calculated self-consistently for a SC (solid line), BCC (dashed line) and FCC (dotted line) structure in a (a) linear and (b) logarithmic scale. The number of $\mathbf{k}$-points used for the calculations was 10^6. The results correspond to a half-filling, nearest-neighbour hopping regime with hopping parameter equal to unity, where $\mathcal{D}_{\mathrm{BCC}}(E_{\mathrm{F}}) > \mathcal{D}_{\mathrm{SC}}(E_{\mathrm{F}}) > \mathcal{D}_{\mathrm{FCC}}(E_{\mathrm{F}})$ holds, which is why the order parameters satisfy $\Delta_{\mathrm{BCC}} > \Delta_{\mathrm{SC}} > \Delta_{\mathrm{FCC}}$ for every value of Λ.

order parameter is 4 to 6 orders of magnitude smaller compared to Λ for the SC and FCC structures in the range $0.0 < \Lambda \leq 0.55$. As the coupling constant increases, Λ/Δ decreases and for $\Lambda > 1.15$ we find $\Lambda/\Delta = \mathcal{O}\left(10^2\right)$ for the SC and FCC structures and $\Lambda/\Delta = \mathcal{O}(10)$ for the BCC structure. For reference, theoretical studies [36] have shown that $\Lambda/\Delta = \mathcal{O}\left(10^3\right)$ for bulk Nb, which has a relatively large average superconducting gap, equal to 1.56 meV [37]. We may therefore consider all induced gaps for $\Lambda > 1.15$ as unrealistic. Of course, this does not stop us from choosing such values for Λ whenever we want an artificially large gap, allowing us to see in-gap states with a satisfactory resolution.

3.2 Superconducting Surfaces

Many of the systems studied in this thesis consist of impurities embedded in or adsorbed on the surface of superconductors. However, as mentioned in Section 2.4, surfaces and interfaces cannot be treated using Bloch's theorem, since they are not periodic along the axis that is normal to the surface plane. A computational workaround is to model a slab, which consists of consecutive atomic layers stacked along one axis (see Appendix A.2). Fig. 3.2 shows the results of a self-consistent calculation for the relative change of (a) the charge and (b) the order parameter of each layer, for a slab with a total of 100 layers, with point of reference the charge and order parameter of the slab's middle layer. The parameters used for this calculation are $\varepsilon_i = 0.0$, $U_i = 0.0$, $\bar{n}_i = 1.0$ and $\Lambda_i = 2.1$, for all layers, and $T = 5 \cdot 10^{-4}$ for the temperature.

Clearly, both the charges and the order parameters show spatial modulations in the form of standing-wavelike perturbations that decay with distance from the surface. The effect is more prominent for the order parameters, since this oscillatory behaviour appears at the 6th decimal for the charges. However, in both cases, the charges and order parameters in the

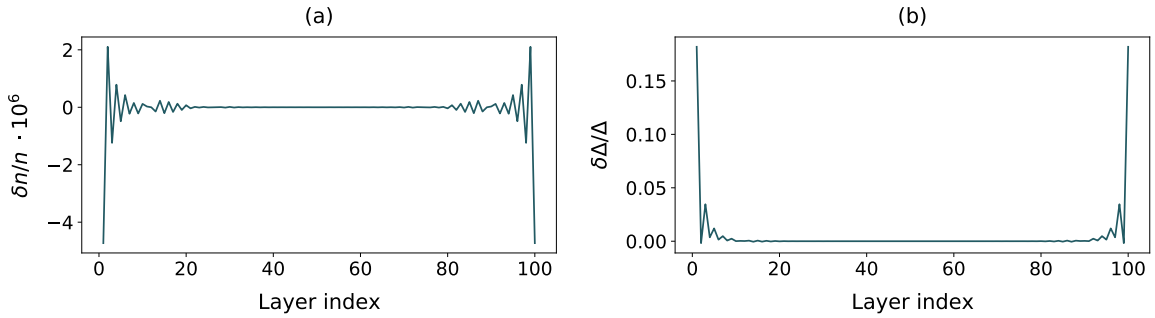

Figure 3.2: Relative change of the (a) charge and (b) order parameter for each atomic layer in a 100-layer slab with $\bar{n}_i = 1.0$, with the middle layer's charge and order parameter as a point of reference. In both cases, a spatial standing-wavelike oscillatory behaviour is seen, which decays with distance from the surface and completely disappears between the 20th and 80th layer. This effect appears at the 6th decimal of the charges.

middle region of the slab are uniform, since the oscillations do not practically extend beyond the 20th and 80th layer.

This is an effect analogous to Friedel oscillations in metals, where the charges experience spatial oscillations in the form of a standing wave due to the boundary condition of a defect (an impurity, an interface or a surface) that breaks the translational symmetry of the crystal potential. The wavevector corresponding to Friedel oscillations is $2k_{\mathrm{F}}$, where k_{F} is the Fermi wavevector, which means that they are dependent on the shape of the Fermi surface. In directions in reciprocal space where the Fermi level happens to fall in a band gap, holes appear in the Fermi surface and therefore a complex value can be assigned to k_{F}, leading to an exponential decay of the spatial modulation of the charges, superimposed with the oscillatory behaviour thereof. Within the tight-binding simple-cubic model with nearest-neighbour hopping, the Fermi surface is topologically equivalent to a sphere for small values of the Fermi energy, however as the Fermi level increases holes start to form in the [100], [010] and [001] directions. We therefore expect that decreasing the chemical potential (which is equivalent to decreasing the value of $\bar{n}_i$ for all layers) will lead to the enhancement of the Friedel-like oscillations across the slab.

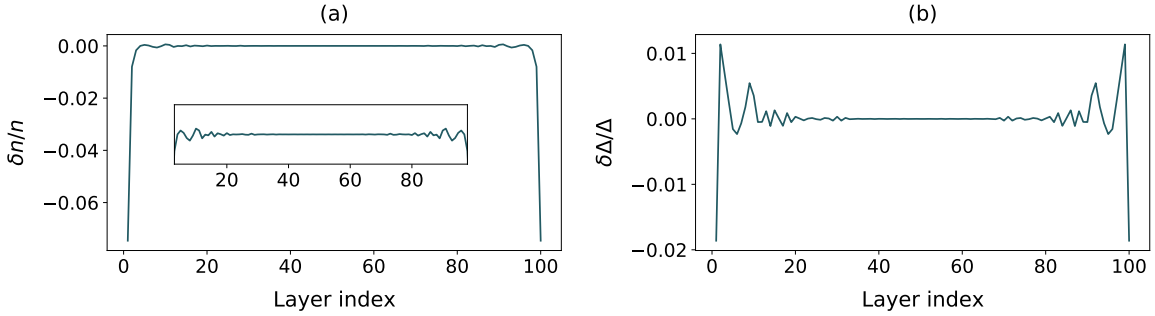

Figure 3.3: Relative change of the (a) charge and (b) order parameter for each atomic layer in a 100-layer slab with $\bar{n}_i = 0.4$, with the middle layer's charge and order parameter as a point of reference. The inset in diagram (a) depicts the charges for layers 3-98. The Friedel-like oscillations are enhanced, compared to the case $\bar{n}_i = 1.0$, since they extend beyond the 20th and 80th layer and also appear at the third decimal of the charges.

Fig. 3.3 shows the results of the self-consistent calculations for the slab using the same parameters, with the exception of the desired charge per atom, which is taken $\bar{n}_i = 0.4$ for all layers. As expected, the resulting Friedel-like oscillations extend beyond the 20th and 80th layer and appear at the third decimal of the charges.

3.3 Non-Magnetic Impurities

Having modelled superconducting surfaces, we may move on to the main purpose of this thesis, which is to study the effects of impurities embedded in or adsorbed on them. As already mentioned, impurities are also a source of Friedel oscillations in metals. Fetter [38] was the first to theoretically study the impact of non-magnetic impurities embedded in superconductors, considering a hard-sphere impurity in a 3-dimensional superconducting host. He demonstrated that a self-consistent treatment of the gap equation leads to Friedel-like oscillations of the charge and order parameter.

In order to prove the validity of this statement for our model, we use the results obtained in Section 3.2 for the superconducting slab with $\bar{n}_i = 0.4$ for all layers and introduce a non-magnetic impurity by replacing a host atom from the topmost layer with an atom with $\Lambda = 0$ and $\varepsilon = -0.5$. Supposing that the slab consists of Nb monolayers, the non-magnetic impurity may correspond to a Ru atom, which is characterized by a larger number of valence electrons. An important remark that has to be made at this point is that our model does not allow for different hopping parameters for the impurities, compared to the hopping parameters for the host atoms [see Eq. (2.46)]. Therefore, our choice of Ru is not made only due to it being non-magnetic, but also because its valence electrons occupy d-orbitals, just like the valence electrons of Nb, and thus the parameters for the hoppings Nb $\leftrightarrow$ Nb and Nb $\leftrightarrow$ Ru are not expected to be considerably different.

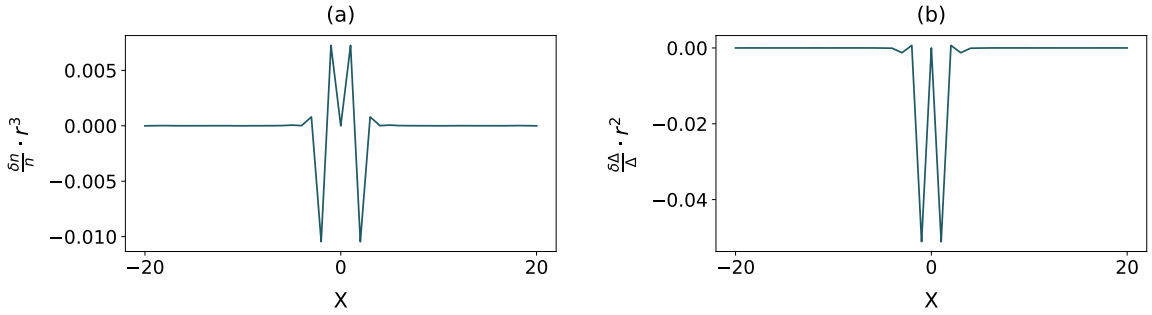

Figure 3.4: Friedel-like oscillations for (a) the charges and (b) the order parameters. The integer X is the position of each atom along the x-axis measured in lattice constants, with $X = 0$ corresponding to the impurity site. The oscillations practically do not extend beyond $X = \pm 5$, due to the large value of Δ.

Fig. 3.4 shows the relative variation of (a) the charges and (b) the order parameters, multiplied by a power of r, which is the distance from the impurity, for 41 atoms in the topmost surface layer. X corresponds to the position of each atom along the x-axis, with the impurity

lying on $X = 0$. Clearly, the existence of Friedel-like oscillations is confirmed, however they decay very fast and do not extend beyond $X = \pm 5$. In Fetter's work, the relative variation of the charges and order parameters falls off as

$$\frac{\delta n}{n} \equiv \frac{n^{\text{imp}} - n^{\text{host}}}{n^{\text{host}}} \propto \frac{\exp(-r\Delta)}{r^3} \tag{3.2}$$

and

$$\frac{\delta \Delta}{\Delta} \equiv \frac{\Delta^{\text{imp}} - \Delta^{\text{host}}}{\Delta^{\text{host}}} \propto \frac{a}{r^3} + \frac{b \cdot \exp(-r\Delta)}{r^2} \tag{3.3}$$

respectively, where a and b are system-dependent constants. Apart from a polynomial decay, there is also an exponential decay that depends on the gap size, thus explaining the dramatic decay of the oscillations, if one takes into account that the gap sizes considered in our simulations are very large compared to realistic gap values. Of course, Eqs. (3.2) and (3.3) can't accurately describe our model[(1)], however their qualitative predictions are not expected to be significantly different.

Aside from inducing Friedel-like oscillations, non-magnetic impurities do not significantly affect the bulk gap or lead to the formation of in-gap states. This is owing to the fact that they act as simple potential scatterers and therefore the pairing mechanism is unaffected, since it is described by an isotropic potential in our model[(2)]. To demonstrate this, we calculate the LDoS at the impurity site.

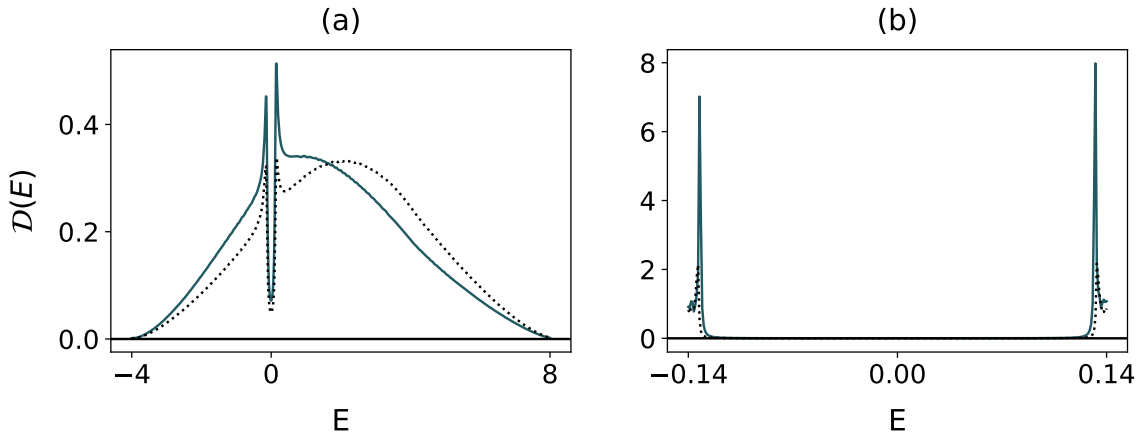

Figure 3.5: LDoS at the impurity site for energies lying (a) in the whole bandwidth and (b) within the superconducting gap. The solid (dotted) lines correspond to the impurity (host) LDoS. The intrinsic linewidth of the energies is taken equal to $\eta = 3 \cdot 10^{-2}$, which is why the gap doesn't appear at exactly zero energy in the full-bandwidth LDoS.

(1) For example, the slab is not equivalent to an isotropic 3-dimensional system and therefore the power laws r^{-3} and r^{-2} would need to be modified.

(2) The gap could be greatly affected by the presence of non-magnetic impurities in unconventional superconductors with anisotropic pairing mechanisms [39].

In Fig. 3.5 the solid (dotted) lines correspond to the impurity (host) LDoS. For the full-bandwidth LDoS diagrams shown in Fig. 3.5 (a), while the two diagrams are different, owing to the presence of the impurity, the gap's features indeed appear unaffected. Fig. 3.5 (b) shows the LDoS calculated for energies in the interval $-0.14 \leq E \leq 0.14$. This choice is due to the fact that the order parameter corresponding to the uppermost layer converges at $\Delta \simeq 0.14$, so it allows us to focus only on energies that lie inside the superconducting gap and demonstrate that no in-gap states exist. In contrast, the impurity seems to simply enhance the spectral density of the gap's peaks at $E = \pm\Delta$, which is consistent with the fact that the self-energy parameter ε for the impurity is negative, thus drawing the DoS maximum closer to the gap.

3.4 Magnetic Impurities

As we've established, the presence of non-magnetic impurities on the surface of superconductors has no significant impact on the bulk superconducting gap, due to the isotropic nature of the superconducting pairing mechanism. On the contrary, magnetic impurities locally break the superconductors' time-reversal symmetry (TRS). Since s-wave superconductivity arises from spin-singlet Cooper pairs, magnetism and superconductivity are competitive phenomena and therefore magnetic impurities can greatly impact the gap and even make it vanish when the impurities' concentration becomes very large. In order to acquire some insight into how magnetic impurities affect a superconducting system, let us suppose that H_0 from Eq. (2.11) describes a bulk superconductor, where $\mathbf{B}_i = \mathbf{0}$ and $U_i = 0$, for every atom i. For simplicity, we shall first consider only a single magnetic impurity, described by the on-site Hamiltonian δH, where

$$\delta H = -J_i \sum_{\sigma\sigma'} c^\dagger_{i\sigma} \left(\boldsymbol{\sigma} \cdot \mathbf{S}_i\right)_{\sigma\sigma'} c_{i\sigma'} \ . \tag{3.4}$$

Here, i is a collective index corresponding to the lattice and atom site of the impurity, J_i is the interaction strength and $\mathbf{S}_i$ is the impurity spin. This Hamiltonian describes the exchange interaction of a conduction band electron with the impurity spin. To further simplify the problem, we may treat the impurity in the classical limit, where the spin is assumed to be large ($|\mathbf{S}_i| \to \infty$) and the interaction strength small ($J_i \to 0$), while their product remains finite. This is equivalent to treating the magnetic impurity's spin as a "frozen" magnetic moment and completely ignoring spin-fluctuations due to its quantum mechanical nature. In this case, one may set $\mathbf{B}_i = (J\mathbf{S})_i$ in order to confirm that the magnetic impurity's Hamiltonian resembles the second term of the RHS of Eq. (2.5).

This model and some of its variations were first studied by Yu, Shiba and Rusinov [41–43]. They found that the exchange interaction of the impurity's spin with the incident bulk electron's spin, which participates in a Cooper pair, energetically favours the breaking of that pair and a new bound state with lower energy is formed at the impurity site. Such

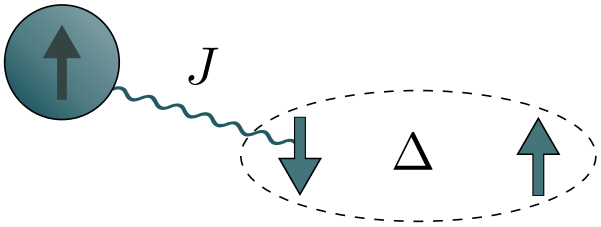

Figure 3.6: Schematic representation of the magnetic impurity's interaction with a Cooper pair [40].

bound states are called Yu-Shiba-Rusinov (YSR) states. Each YSR state has an electron-like component with energy E_{YSR} and a hole-like component with energy $-E_{\mathrm{YSR}}$ and therefore its appearance is indicated by the presence of two resonances in the LDoS at $\pm E_{\mathrm{YSR}}$[(3)]. In this simple model, E_{YSR} is calculated to be [43]

$$E_{\mathrm{YSR}} = \Delta \frac{1 - \left[\pi \mathbf{B}_i \mathcal{D}\left(E_{\mathrm{F}}\right)\right]^2}{1 + \left[\pi \mathbf{B}_i \mathcal{D}\left(E_{\mathrm{F}}\right)\right]^2}, \tag{3.5}$$

where $\mathcal{D}\left(E_{\mathrm{F}}\right)$ is the density of states at the Fermi level in the normal state and Δ is the order parameter in the vicinity of the impurity. This expression makes evident the fact that YSR states lie inside the superconducting gap, since $E_{\mathrm{YSR}} < \Delta$.

In order to illustrate the existence of in-gap YSR states, we use the same superconducting slab with $\bar{n}_i = 0.4$ and we substitute one atom from the uppermost layer with a magnetic impurity, by setting $\Lambda = 0.0$ and $\mathbf{B} = 1.0\ \hat{\mathbf{z}}$ at the impurity site. Supposing that the superconducting surface corresponds to Nb monolayers, the substitutional impurity may correspond to V, which is a magnetic atom with valence electrons on d-orbitals, thus justifying our approximation of common hopping elements. In addition, V is isoelectronic to Nb, which is why the impurity's desired charge and self-energy are the same as the host atoms', however other magnetic elements, such as Co or Fe, could be considered by properly altering the parameters ε and $\mathbf{B}$. The results of the self-consistent solution of the impurity problem are shown in the LDoS diagrams of Fig. 3.7.

Fig. 3.7 (a) depicts the full-bandwidth LDoS, while Fig. 3.7 (b) shows the LDoS only for energies lying inside the gap. The solid lines in the diagrams correspond to the impurity LDoS, while the dotted lines correspond to the pristine host LDoS at the surface layer. As in the case of the non-magnetic impurity, the presence of the impurity leads to a modification of the LDoS. However, unlike in the non-magnetic case, the appearance of an in-gap YSR state is confirmed by the presence of the two resonances lying symmetrically around zero at $E = \pm 0.091$. The spectral densities of the two resonances are not equal, with the spectral density corresponding to the particle-like peak appearing about three times higher compared to the spectral density corresponding to the hole-like peak. This is due to the fact that the studied system's normal state energy spectrum is not symmetric around zero, thus creating

(3) Note that, despite the fact that two resonances appear in the LDoS, they both belong to the same YSR state.

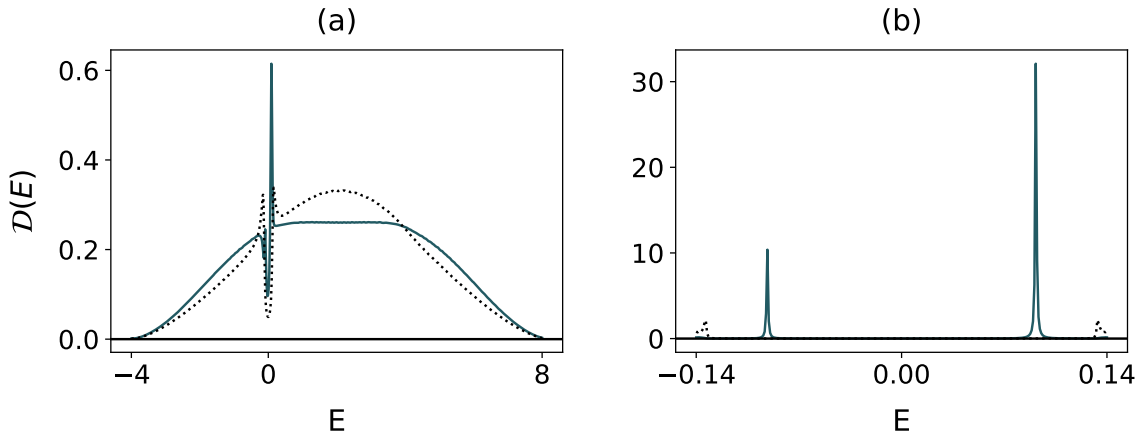

Figure 3.7: LDoS at the impurity site for energies lying (a) in the whole bandwidth and (b) within the superconducting gap. The solid (dotted) lines correspond to the impurity (host) LDoS. The intrinsic linewidth of the energies is taken equal to $\eta = 3 \cdot 10^{-2}$ for the full-bandwidth LDoS and equal to $\eta = 5 \cdot 10^{-4}$ for the in-gap LDoS. The two resonant peaks inside the gap indicate the existence of a YSR state.

an imbalance in the particle-hole sector[(4)]. If the slab had been calculated taking $\bar{n}_i = 1.0$ for all layers (half-filling), the system's chemical potential would have converged to zero. In that case, the normal state's DoS would have been symmetric around zero and therefore the two resonances would have had equal spectral weights. Let us note here that, apart from the exchange term, the impurity Hamiltonian (3.4) could also contain a local Coulomb interaction, analogous to that studied in Section 3.3. In that case, the expression for E_{YSR} would be different, however the two resonances would still lie inside the gap, symmetrically around zero, and the only important difference is that their spectral densities would be further modified[44].

As Eq. (3.5) indicates, the location of the two YSR resonances depends on our choice of $\mathbf{B}$. By continuously varying the effective magnetic field's magnitude, the two peaks will start approaching each other and at some point converge into a common peak at $E = 0$. Further increasing the magnitude of $\mathbf{B}$ will lead to the two peaks "switching sides", with the peak that previously corresponded to the particle-like component of the YSR state becoming the hole-like component thereof and vice versa. To demonstrate that, we solve the impurity problem self-consistently for magnetic field magnitudes B in the range $0.0 \leq B \leq 4.0$ and calculate the spectral density at the impurity site for energies inside the superconducting gap. As can be seen from the LDoS diagrams in Fig. 3.5 (a) and Fig. 3.7 (a), the system's energy bandwidth is equal to 12, therefore our choice for the domain of B is reasonable. The results of the calculations are shown in Fig. 3.8. Indeed, the two peaks are initially located close to the gap edges and as B increases their distance decreases until for $B = 2.16$ there is an overlap of the two peaks. For $B > 2.16$, the two peaks are once again separated, but now

(4) This is the other use of the term particle-hole symmetry mentioned in footnote (2) of Chapter 2.

the peak with the higher (lower) spectral density corresponds to the hole-like (particle-like) component of the YSR state.

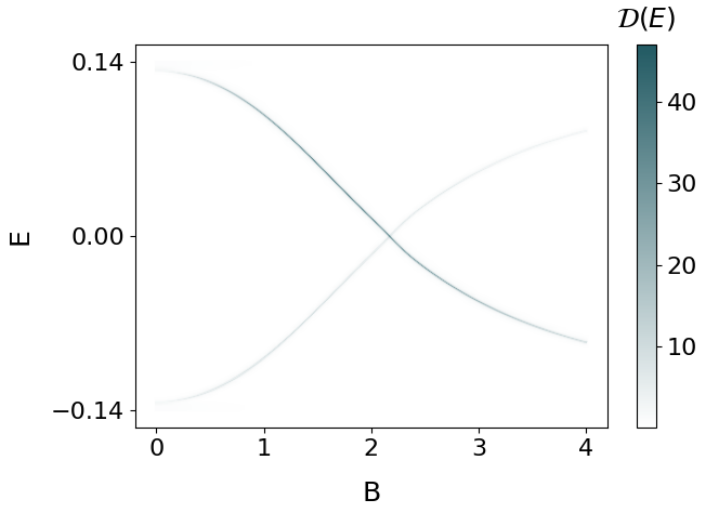

Figure 3.8: Colormap of the spectral density at the impurity site as a function of the local magnetic field's magnitude, for energies $-0.14 \leq E \leq 0.14$. The crossing of the two lines corresponds to a quantum phase transition in the quantum spin model.

Interestingly, the point where the two peaks overlap corresponds to a quantum phase transition[40]. In the case of quantum spins with $S = 1/2$, the transition occurs due to a change of the ground state's fermion parity and the system's total spin changes from $S = 1/2$ to $S = 0$. An important question that therefore needs to be addressed is whether or not the assumption that the finite spin of magnetic atoms such as V can be treated as a frozen magnetic moment is an oversimplification, potentially leading to ambiguous physical results. Indeed, our model is restricted to a classical description of single localized magnetic impurities. Nevertheless, recent spin-polarized scanning tunneling microscopy (STM) studies have shown that exchange-coupling a few spins to larger ensembles via strong isotropic ferromagnetic[45] or antiferromagnetic[46,47] Heisenberg exchange interactions enhances the spin stability of the system. Specifically, spin dynamics have appeared to be greatly suppressed in magnetic chains consisting of only as few as five or six Fe atoms. This means that if one considers specific configurations of arrays instead of single magnetic impurities, the classical treatment of frozen spins is adequate. Of course, for higher concentrations of magnetic impurities, the number of induced YSR states increases and in this way an impurity band is formed inside the gap. As their concentration further increases, the impurity spins yield a gradual reduction of the superconducting gap, which eventually closes. Taking everything into consideration, our next goal is to study arrays of magnetic impurities and investigate whether the system can be driven to a topologically non-trivial state, whilst preserving the bulk gap.

4 Topological Superconductivity

As has already been mentioned, what makes a superconducting system topological (i.e. topologically non-trivial) is the appearance of MZMs at its boundaries. However, being able to tell whether or not a given Hamiltonian describes a topological system requires a well-defined topological invariant. This quantity must be constant under continuous deformations of the system's Hamiltonian, as long as the system remains gapped throughout that process. A closing of the gap is not a sufficient condition for the topological invariant to change, however it is a necessary one. A change in the topological invariant's value accompanied by a reopening of the gap indicates a topological phase transition. Our studied system is the superconducting slab with an array of magnetic impurities embedded on its uppermost layer along the x-axis (Fig. 4.1). The magnetic atoms' spins rotate around the y-axis by a constant angle θ between consecutive spins, thus creating a 1-dimensional non-collinear spin chain. The limiting cases $\theta = 0$ and $\theta = \pi$ correspond to a ferromagnetic and antiferromagnetic configuration, respectively.

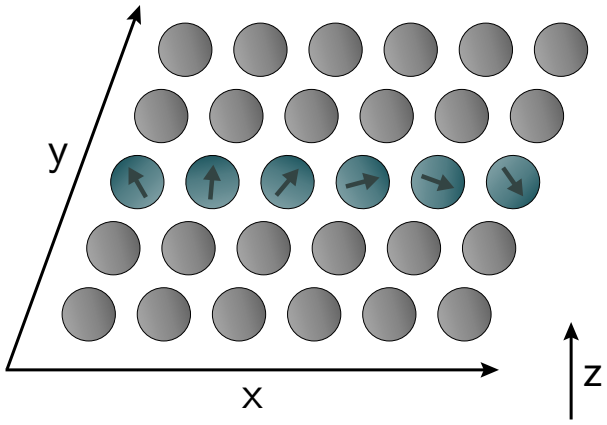

Figure 4.1: A 1-dimensional non-collinear spin chain embedded on the surface of a superconductor.

The question at hand is whether or not the non-collinear spin chain corresponds to a 1-dimensional TSC, for some configuration of the system's parameters. The topological invariant defined for such 1-dimensional systems is known as the Majorana number, $\mathcal{M}$. In order to understand what this number is and why it is a suitable choice, we shall briefly review the simplest case of a TSC: the Kitaev chain.

4.1 The Kitaev Chain

The Kitaev chain is a 1-dimensional model given by the tight-binding Hamiltonian [48]

$$H_{\mathrm{K}} = -\sum_{\alpha=1}^{N} \mu \left(c_\alpha^\dagger c_\alpha - \frac{1}{2} \right) + t \left(c_\alpha^\dagger c_{\alpha+1} + c_{\alpha+1}^\dagger c_\alpha \right) + \Delta \left(c_\alpha^\dagger c_{\alpha+1}^\dagger + c_{\alpha+1} c_\alpha \right), \tag{4.1}$$

with $t, \Delta \geq 0$, which describes a system of spinless fermions, interacting via a superconducting pairing mechanism that couples nearest neighbours, usually referred to as p-wave superconductivity. At first glance, concepts such as spinless fermions and intra-site superconductivity might seem unphysical or abstract, however during the past two decades literature has been enriched with proposals on how to physically realize this model [18,19,22]. These studies go beyond the purpose of our current analysis, so we shall proceed without getting into a detailed discussion. Let us perform the unitary transformation

$$\begin{pmatrix} b_{2\alpha-1} \\ b_{2\alpha} \end{pmatrix} = \frac{1}{\sqrt{2}} \begin{pmatrix} 1 & 1 \\ -\mathrm{i} & \mathrm{i} \end{pmatrix} \begin{pmatrix} c_\alpha \\ c_\alpha^\dagger \end{pmatrix}, \tag{4.2}$$

where the newly defined operators satisfy $b = b^\dagger$ and $\{b_\alpha, b_{\alpha'}\} = \delta_{\alpha\alpha'}$. This indicates that the above transformation replaces each "complex" fermion by two "real" Majorana fermions, corresponding to the hermitian and anti-hermitian part of the complex fermion, thus doubling the system's degrees of freedom. For this reason, this representation of fermionic operators is known as the Majorana representation. In terms of the Majorana operators, the Hamiltonian is written as

$$H_{\mathrm{K}} = \mathrm{i} \sum_{\alpha=1}^{N} -\mu b_{2\alpha-1} b_{2\alpha} + \mathrm{i} \sum_{\alpha=1}^{N-1} (t+\Delta)\, b_{2\alpha} b_{2\alpha+1} + (\Delta - t)\, b_{2\alpha-1} b_{2\alpha+2}. \tag{4.3}$$

Notice that the second summation is taken over $\alpha = 1, \ldots, N-1$, because there are no b_{2N+1} or b_{2N+2} Majorana operators. An observation that will be useful later on is that Eq. (4.3) has the form

$$H_{\mathrm{K}} = \mathrm{i} \sum_{i,j} b_i A_{ij} b_j, \tag{4.4}$$

where $\boldsymbol{A}$ is a real $2N \times 2N$ matrix, which is also skew-symmetric, because H_{K} is hermitian.

We will now study two special limits of this system. The first corresponds to $\Delta = 0 = t$ and $\mu < 0$. The Hamiltonian then reduces to

$$H_{\mathrm{K}} = \mathrm{i}\,(-\mu) \sum_{\alpha=1}^{N} b_{2\alpha-1} b_{2\alpha} = -\mu \sum_{\alpha=1}^{N} \left(c_\alpha^\dagger c_\alpha - \frac{1}{2} \right), \tag{4.5}$$

which describes a system where the Majorana fermions pair up on the same site [see Fig. 4.2 (a)]. In the last equation we have momentarily restored the complex fermionic operators using Eq. (4.2), to illustrate the fact that the ground state of this system is the vacuum $|0\rangle_c$ of the spinless fermions corresponding to the c operators. The system is gapped, since adding one such fermion into it costs a finite energy $|\mu|$.

In order to study the other limit, we take $\Delta = t$ and $\mu = 0$, so the Hamiltonian becomes

$$H_{\mathrm{K}} = \mathrm{i}t \sum_{\alpha=1}^{N-1} b_{2\alpha} b_{2\alpha+1}. \tag{4.6}$$

This corresponds to a system where the Majorana fermions from neighbouring sites are paired together, while the Majorana fermions at the ends of the chain are left unpaired [see Fig. 4.2 (b)]. It is natural to define new complex fermionic operators to describe the new Majorana pairs. For that purpose, we write

$$\begin{pmatrix} d_\alpha \\ d_\alpha^\dagger \end{pmatrix} = \frac{1}{\sqrt{2}} \begin{pmatrix} 1 & \mathrm{i} \\ 1 & -\mathrm{i} \end{pmatrix} \begin{pmatrix} b_{2\alpha} \\ b_{2\alpha+1} \end{pmatrix} \tag{4.7}$$

and the Hamiltonian is transformed to

$$H_{\mathrm{K}} = t \sum_{\alpha=1}^{N-1} \left(d_\alpha^\dagger d_\alpha - \frac{1}{2} \right). \tag{4.8}$$

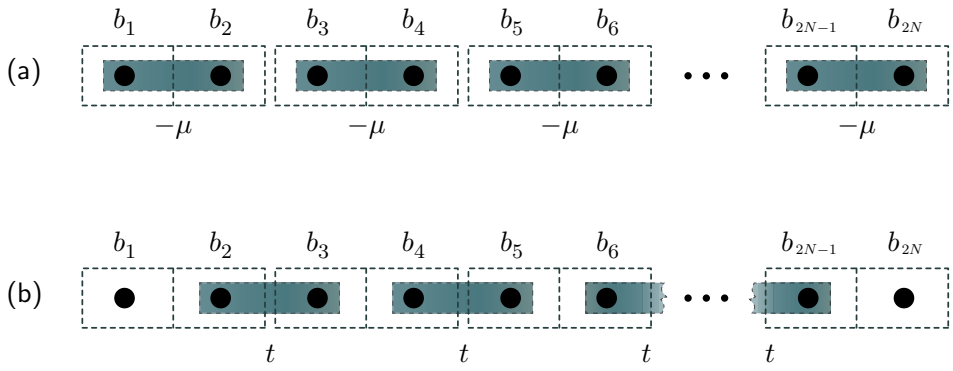

Figure 4.2: The two different coupling regimes, with (a) corresponding to $\Delta = 0 = t$ and $\mu < 0$ and (b) to $\Delta = t$ and $\mu = 0$.

As it becomes evident, the ground state of this system is the vacuum of the fermions corresponding to the d operators. Furthermore, the "bulk" of the chain is gapped, since adding one such fermion into the system costs a finite energy t. However, there is a key difference compared to the previous case, which renders the two vacua topologically inequivalent. This becomes apparent if we define the fermionic operator

$$f = \frac{1}{\sqrt{2}} \left(b_1 + \mathrm{i} b_{2N} \right), \tag{4.9}$$

which is the annihilation operator of a highly non-local fermion, since its constituents are the two Majorana fermions at the ends of the chain. Due to the fact that the operators b_1 and b_{2N} (and therefore f) do not enter the Hamiltonian (4.8), it means that the energy cost of adding a fermion corresponding to f is equal to zero. This is why the Majorana fermions at the chain ends are known as MZMs. As a result, this system's ground state has a two-fold degeneracy, because if $|0,0\rangle_{d,f}$ is a ground state that satisfies $f\,|0,0\rangle_{d,f} = 0$, then so is $|0,1\rangle_{d,f}$, which satisfies $f\,|0,1\rangle_{d,f} = |0,0\rangle_{d,f}$.

Taking everything into account, we are finally able to introduce a topological invariant which allows one to discern the trivial phase, where no MZMs appear at the ends of the chain, from the topological phase. In general, due to the mean-field treatment of superconductivity, the particle number is not a conserved quantity in such systems. However, the fermion parity is, since the correspoding operator commutes with the Hamiltonian. The fermion parity operator for the Hamiltonian (4.6) is

$$Q_1 = \exp\left(\mathrm{i}\pi \sum_{\alpha=1}^{N} c_\alpha^\dagger c_\alpha\right) \tag{4.10}$$

and $Q_1\,|0\rangle_c = +\,|0\rangle_c$, which means that the parity of the ground state is even. This is expected, since all fermions form Cooper pairs. As far as the Hamiltonian (4.8) is concerned, the fermion parity operator is

$$Q_2 = \exp\left[\mathrm{i}\pi\left(\sum_{\alpha=1}^{N-1} d_\alpha^\dagger d_\alpha + f^\dagger f\right)\right] \tag{4.11}$$

and the parity of the ground state $|0,1\rangle_{d,f}$, where MZMs are present at the ends of the chain, is odd, since $Q_2\,|0,1\rangle_{d,f} = -\,|0,1\rangle_{d,f}$. In other words, we may define the Majorana number $\mathcal{M}$ as

$$\mathcal{M} = Q\,(H)\,, \tag{4.12}$$

where $Q\,(H)$ is the parity of Hamiltonian's H ground state. The case $\mathcal{M} = +1$ corresponds to a topologically trivial, while $\mathcal{M} = -1$ corresponds to a topologically non-trivial system.

Eq. (4.12) highlights what is known in the field of topological quantum matter as bulk-boundary correspondence: the existence of MZMs at the ends of the chain (boundary) can be inferred from the system's ground state parity, a property corresponding to its bulk. One may naively think that if we were to close the chain into a loop (imposing periodic boundary conditions), then the information about its topological phase would vanish. What is true, is that closing the chain into a loop would not allow the observation of MZMs, since the b_1 and b_{2N} Majorana fermions would come into proximity and couple into a local fermion (see Fig. 4.3). Howerver, the Majorana number would still be well defined and would provide the information of whether MZMs would appear at the boundaries of the chain, if we "cut it open" at some point.

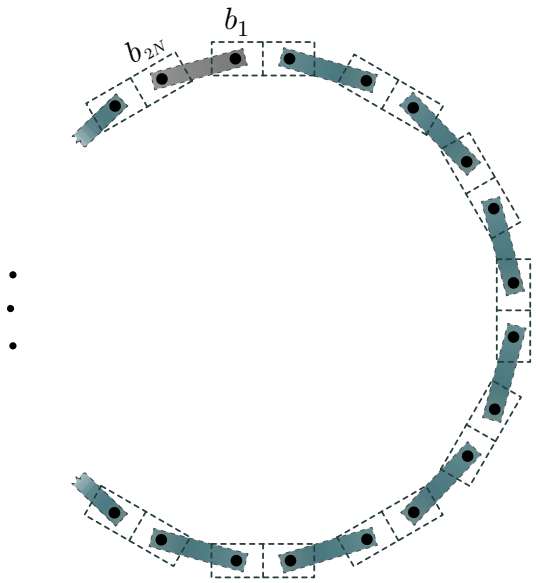

Figure 4.3: Closing the Kitaev chain into a loop leads to the pairing of the end modes.

4.2 The Role of Particle-Hole Symmetry

Admittedly, Kitaev's model seems quite different from our spin chain, so the question risen is whether or not we can use the same topological invariant in order to study the appearance of MZMs in our model. Of course, the whole point of topological equivalence in quantum condensed matter is grouping together seemingly different Hamiltonians, which can be continuously transformed into one another, as long as they remain gapped during the transformation. If we further require that some symmetry be preserved throughout the continuous path that connects the Hamiltonians, then we can group them into symmetry classes. The "tenfold way" is one such classification, where single-particle Hamiltonians are split into ten symmetry classes according to their behaviour under time-reversal, particle–hole and chiral symmetry [49,50]. In this context, the topological equivalence of the Kitaev chain and our model stems from the fact that they are both particle-hole symmetric, due to the redundancy of the BdG formalism. While the BdG formalism was not explicitly applied in the case of the Kitaev chain, the doubling of the system's degrees of freedom by the introduction of Majorana operators gave rise to the same effect of the Hamiltonian's eigenvalues coming in pairs. This can be seen directly from Eq. (4.4), because $\boldsymbol{A}$ is a real, skew-symmetric matrix and therefore its eigenvalues are either equal to zero, or purely imaginary conjugate pairs. If $\{\mathrm{i}\epsilon_n, -\mathrm{i}\epsilon_n\}$, where $n = 1, \ldots, N$ and $\epsilon_n \geq 0$, is the set containing the eigenvalues of $\boldsymbol{A}$, then the Hamiltonian's eigenvalues are the elements of the set $\{\epsilon_n, -\epsilon_n\}$.

At this point, we must note that, apart from PHS, the Kitaev chain also obeys TRS[(1)] and therefore belongs to symmetry class BDI in the tenfold way classification [49,50], unlike our model which is only particle-hole symmetric and therefore belongs to symmetry class D.

[(1)] The Kitaev chain is also chirality symmetric, because, if a single-particle Hamiltonian obeys PHS and TRS, then by default it also obeys chiral symmetry [50].

However, the Kitaev chain's TRS is "accidental", due to the spinless nature of the fermions considered. More realistic models of 1-dimensional p-wave TSCs are not TRS invariant, so we can view the Kitaev chain as a representative of the symmetry class D. In fact, the equivalence of the Majorana number and the topological invariant corresponding to the Hamiltonians of symmetry class D (known as the quantized Zak-Berry phase) has been analytically proven [51].

Returning to Eq. (4.4), a rather important feature of skew-symmetric matrices such as $\boldsymbol{A}$ is that a Pfaffian, $\mathrm{Pf}(\boldsymbol{A})$, can be assigned to them. The rigorous definition of the Pfaffian [52] goes beyond the scope of our discussion, so we will present it in loose terms. Since the eigenvalues of $\boldsymbol{A}$ come in pairs, the determinant of $\boldsymbol{A}$ is equal to

$$\det(\boldsymbol{A}) = \prod_{n=1}^{N} \epsilon_n^2, \tag{4.13}$$

which is always non negative. The key property of the Pfaffian is that it allows to take the square root of the determinant, equal to $\pm \prod \epsilon_n$, in such a way that the sign of the product is uniquely defined. Now, as we've already established, the Majorana number is well defined even in the case of chains with periodic boundary conditions, where no MZMs are present and therefore the system is fully gapped ($\epsilon_n \neq 0$). In that case, Kitaev has shown that the parity of the Kitaev chain's ground state is equal to the sign of $\mathrm{Pf}(\boldsymbol{A})$. As a result, the Majorana number can assume the form

$$\mathcal{M} = \mathrm{sgn}\left[\mathrm{Pf}(\boldsymbol{A})\right]. \tag{4.14}$$

This expression is of great significance, as it implies that one can determine whether a 1-dimensional periodic superconducting system is topological or not, simply by switching into the Majorana representation (which is always possible thanks to PHS) and calculating the sign of $\mathrm{Pf}(\boldsymbol{A})$.

4.3 Majorana Number for the Closed Spin Chain

Returning to our spin chain model, recall that the system's inherent PHS is expressed by the operator $\mathcal{P}$. Suppose that U is a unitary operator with matrix representation $\boldsymbol{U}$, allowing us to switch into a basis $\boldsymbol{\Psi}^n \mapsto \boldsymbol{U} \cdot \boldsymbol{\Psi}^n$, such that

$$\mathcal{P} \mapsto U\mathcal{P}U^\dagger = \mathcal{K}. \tag{4.15}$$

In this transformed basis, the PHS operator is simply the complex conjugation operator. As a result, the symmetry $\mathcal{P}\boldsymbol{\mathcal{H}}^0\mathcal{P}^{-1} = -\boldsymbol{\mathcal{H}}^0$ now becomes

$$\boldsymbol{\mathcal{H}}^{0\,*} = -\boldsymbol{\mathcal{H}}^0. \tag{4.16}$$

This expression implies that the transformed BdG Hamiltonian can be written as

$$\boldsymbol{\mathcal{H}}^0 = \mathrm{i}\,\boldsymbol{\mathcal{A}}, \tag{4.17}$$

where $\boldsymbol{\mathcal{A}}$ is a real, skew-symmetric matrix. This result indicates that the Majorana representation in the BdG formalism is the basis where the PHS operator is equivalent to the complex conjugation operator. Indeed, in this basis Schrödinger's equation (2.21) becomes a real wave equation

$$\boldsymbol{\mathcal{A}} \cdot \boldsymbol{\Psi}^n(t) = \hbar \frac{\partial}{\partial t} \boldsymbol{\Psi}^n(t) \tag{4.18}$$

and as a result the second quantization field operator corresponding to the spinor $\boldsymbol{\Psi}^n$ is formed by a collection of Majorana operators and is self-adjoint.

In reciprocal space, which is where the BdG Hamiltonian is constructed in our computational adaptation (see Section 2.5), the PHS operator is still the complex conjugation operator, since U commutes with the Fourier transform. As one can directly verify from Eq. (2.36), the PHS for the $4N_b \times 4N_b$ BdG Hamiltonian in reciprocal space is expressed by $\widetilde{\boldsymbol{\mathcal{H}}}^{0\,*}(k) = -\widetilde{\boldsymbol{\mathcal{H}}}^{0}(-k)$. This enforces the condition

$$\widetilde{\boldsymbol{\mathcal{A}}}^{*}(k) = \widetilde{\boldsymbol{\mathcal{A}}}(-k) \tag{4.19}$$

for the Fourier transform of $\boldsymbol{\mathcal{A}}_{\alpha\alpha'}$. Notice that the Bloch wavevector is no longer a vector but a real number, as the spin chain is 1-dimensional. Since $\widetilde{\boldsymbol{\mathcal{H}}}^{0}$ is block-diagonal in reciprocal space [Eq. (2.58)],

$$\widetilde{\boldsymbol{\mathcal{A}}} = \bigoplus_k \widetilde{\boldsymbol{\mathcal{A}}}(k) \tag{4.20}$$

must also hold. Using Eq. (4.20), as well as the identity $\mathrm{Pf}(\boldsymbol{A}_1 \oplus \boldsymbol{A}_2) = \mathrm{Pf}(\boldsymbol{A}_1)\,\mathrm{Pf}(\boldsymbol{A}_2)$, the Majorana number becomes

$$\begin{aligned}
\mathcal{M} &= \mathrm{sgn}\left[\mathrm{Pf}\left(\boldsymbol{A}\right)\right] = \mathrm{sgn}\left[\mathrm{Pf}\left(\widetilde{\boldsymbol{\mathcal{A}}}\right)\right] = \\
&= \mathrm{sgn}\left\{\prod_k \mathrm{Pf}\left[\widetilde{\boldsymbol{\mathcal{A}}}(k)\right]\right\} = \\
&= \mathrm{sgn}\left\{\prod_{k=-k} \mathrm{Pf}\left[\widetilde{\boldsymbol{\mathcal{A}}}(k)\right] \prod_{k\neq -k} \det\left[\widetilde{\boldsymbol{\mathcal{A}}}(k)\right]\right\} = \\
&= \mathrm{sgn}\left\{\mathrm{Pf}\left[\widetilde{\boldsymbol{\mathcal{A}}}(k=0)\right] \mathrm{Pf}\left[\widetilde{\boldsymbol{\mathcal{A}}}\left(k=\frac{\pi}{a}\right)\right]\right\},
\end{aligned} \tag{4.21}$$

where a is the lattice constant. In order to arrive at the final equation, we first used the fact that $\mathrm{sgn}\left[\mathrm{Pf}\left(\boldsymbol{\mathcal{A}}\right)\right] = \mathrm{sgn}\left[\mathrm{Pf}\left(\widetilde{\boldsymbol{\mathcal{A}}}\right)\right]$, since the ground state parity is independent of whether we choose the configuration or reciprocal space basis to study the system. Then, using Eq. (4.19) as well as the identity $\mathrm{Pf}\left(\boldsymbol{A}\right)^2 = \det\left(\boldsymbol{A}\right)$, we grouped together the $\{k, -k\}$ pairs[(2)]. However, since the eigenvalues of $\widetilde{\boldsymbol{\mathcal{A}}}\left(k\right)$ are equal to -i times the eigenvalues of $\widetilde{\boldsymbol{\mathcal{H}}}^0\left(k\right)$, the sign of $\det\left[\widetilde{\boldsymbol{\mathcal{A}}}\left(k\right)\right]$ is positive. Finally, since $k = 0$ and $k = \pi/a$ are the only points in the Brillouin zone that are mapped onto themselves by $k \to -k$, they are the only points relevant for the calculation of the Majorana number.

Even though the spin chain itself is 1-dimensional, the full system is not, as the chain cannot be separated from the surface it is embedded on. However, by defining a large enough supercell (see Appendix A.3) as the system's unit cell, we can model the full system as an effective 1-dimensional one. Afterwards, imposing periodic boundary conditions along the chain's axis allows us to calculate the $\widetilde{\boldsymbol{\mathcal{A}}}\left(k\right)$ matrix and thus determine the Majorana number for various configurations of the system's parameters. Finally, for any point of parameter space where $\mathcal{M} = -1$, we may proceed to study the open chain using Green functions formalism in order to confirm or disprove the existence of MZMs. For the reciprocal space BdG Hamiltonian given by Eq. (2.56), by demanding that the matrix $\boldsymbol{U}$ be unitary and that it also satisfy Eq. (4.15), we calculate it to be

$$\boldsymbol{U} = \frac{1}{2}\begin{pmatrix} \mathbf{I} & 0 & -\mathbf{I} & 0 \\ 0 & \mathbf{I} & 0 & \mathbf{I} \\ 0 & -\mathbf{I} & 0 & -\mathbf{I} \\ \mathbf{I} & 0 & -\mathbf{I} & 0 \end{pmatrix} + \frac{\mathrm{i}}{2}\begin{pmatrix} 0 & \mathbf{I} & 0 & -\mathbf{I} \\ \mathbf{I} & 0 & \mathbf{I} & 0 \\ \mathbf{I} & 0 & \mathbf{I} & 0 \\ 0 & -\mathbf{I} & 0 & \mathbf{I} \end{pmatrix}, \tag{4.22}$$

where $\mathbf{I}$ is the N_b-dimensional identity matrix. Following Nadj-Perge et. al[26], we are interested in investigating whether a topological phase exists for the spin chain in the cases (a) $\theta = 0$, (b) $\theta = \pi$ and (c) $\theta = 2\pi/3$. The latter corresponds to a spin helix, where the spins along the x-axis perform a full rotation every 3 magnetic impurities. For this purpose, we model the superconducting surface by solving the BdG equations self-consistently for 100 layers, choosing $\Lambda_i = 2.1$, $\bar{n}_i = 0.4$, $\varepsilon_i = 0.0$ and $U_i = 0.0$ for all atoms and $T = 5 \cdot 10^{-3}$ for the temperature. We then replace host atoms with magnetic impurities, setting $\Delta_{\alpha i} = 0$ at the impurity positions and assume that the magnitudes of their local magnetic fields, B, are equal. Finally, we continuously vary each system's Hamiltonian with respect to the magnitude of the magnetic impurities' local magnetic field, while all other parameters are kept constant, in order to calculate the Majorana number for each value of B. The results shown in Fig. 4.4 correspond to $0.0 \leq B \leq 4.0$ and were obtained by including M. Wimmer's Algorithm 923[52] for the calculations of the Pfaffians in our code.

---

(2) Notice that if $\{\mathrm{i}\epsilon_n, -\mathrm{i}\epsilon_n\}$ is the set containing the eigenvalues of $\boldsymbol{\mathcal{A}}$, then the same set corresponds to the eigenvalues of $\boldsymbol{\mathcal{A}}$. As a result, $\mathrm{Pf}\left[\widetilde{\boldsymbol{\mathcal{A}}}\left(k\right)\right] = \mathrm{Pf}\left[\widetilde{\boldsymbol{\mathcal{A}}}^*\left(k\right)\right]$ holds.

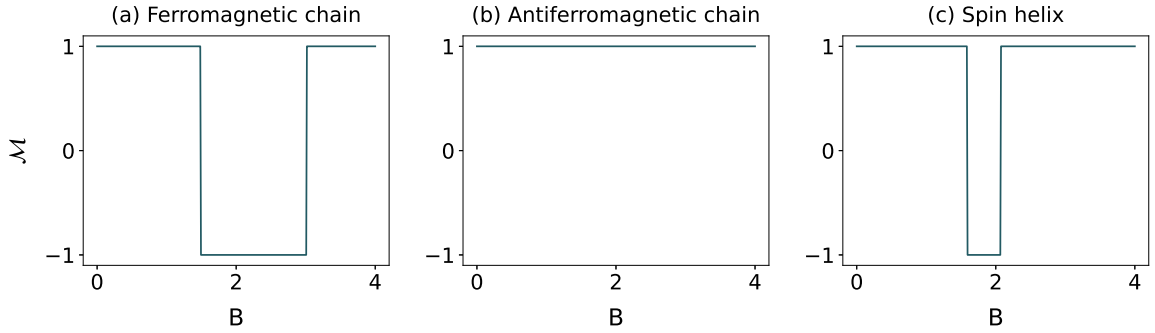

Figure 4.4: Calculation of the Majorana number for (a) the ferromagnetic, (b) the antiferromagnetic and (c) the spin helix configuration for $0.0 \leq B \leq 4.0$. The parameters for the plots are as follows: $\Lambda_i = 2.1$, $\bar{n}_i = 0.4$, $\varepsilon_i = 0.0$, $U_i = 0.0$ and $T = 5 \cdot 10^{-3}$. No topological phase seems to exist in case (b), however cases (a) and (c) yield promising results.

Clearly, no topological phase exists in the case of the antiferromagnetic chain, since $\mathcal{M} = +1$ for all values of B. On the other hand, the Majorana number is $\mathcal{M} = -1$ in the domain $1.50 \leq B \leq 3.00$ for the ferromagnetic chain and in the domain $1.60 \leq B \leq 2.07$ for the spin helix. One may naively think that we have successfully identified topologically non-trivial phases for cases (a) and (c), however we still need to confirm that a bulk gap in which the candidate MZMs are localized still exists once we cut each chain open.

4.4 Opening the Chain

In order to study the open chain, we keep the same values for all parameters in the BdG self-consistency scheme and replace 30 host atoms from the uppermost layer with magnetic impurities. For the ferromagnetic chain all spins are aligned along the z-axis, while for the spin helix the first spin is aligned along the x-axis and there is a total of 10 full spin rotations along the chain. To investigate if the chains host MZMs at their edges, we perform one-shot calculations of the spectral densities of the impurities at the ends of the chains for energies in the interval $-0.14 \leq E \leq 0.14$. Based on the results shown in Fig. 4.4, we study the systems for values of the local magnetic fields in the range $1.0 \leq B \leq 3.0$. The results are shown in Fig. 4.5.

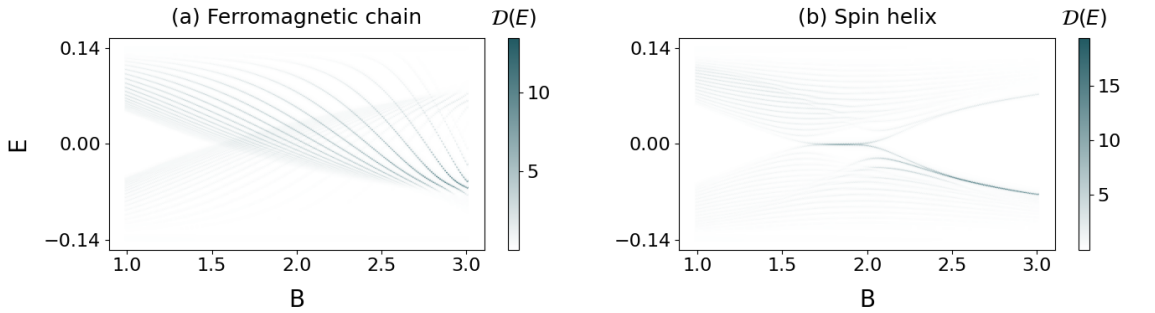

Figure 4.5: The intensity at each point corresponds to the spectral density of the atoms located at the chain ends for energies $-0.14 \leq E \leq 0.14$ and local magnetic field magnitudes $1.0 \leq B \leq 3.0$. For both diagrams the impurity problem was solved for chains consisting of 30 impurities, with (a) corresponding to a ferromagnetic and (b) corresponding to a spin helix configuration.

The first important remark that can be made is that in both cases, for several values of B, we find $\mathcal{D}(E=0) \neq 0$, however, in contrast to what can be seen in diagram (b), the spectral densities at $E \neq 0$ but still in the vicinity of $E = 0$ are non zero in diagram (a). This is an indication that the ferromagnetic chain is gapless in the region where $\mathcal{M} = -1$, while a gap is preserved in the spin helix, with a single, isolated, localized state appearing at $E = 0$. The second significant observation is that the spectral density in the vicinity of $E = 0$ for the ferromagnetic chain is very different compared to the spin helix, where $\mathcal{D}(E=0) \gg \mathcal{D}(E \neq 0)$ in the domain $1.73 \leq B \leq 1.93$. Let us note here that the domain of B in which a topological phase is present has a smaller radius compared to the results obtained from the Majorana number calculations. This can be attributed to the fact that, due to computational limitations for the calculation of the Majorana number, we are unable to define a supercell large enough to accurately reduce the 3-dimensional problem to a 1-dimensional one. Another possible explanation for this could be the fact that the closed chain is infinite in length, while the open chain consists of only 30 atoms and is therefore only an approximation of the infinite chain problem.

The conclusion that can be drawn is that the only chain that exhibits a topological phase is the spin helix. In order to illustrate this, we choose $B = 1.8$, for which $\mathcal{M} = -1$ and $\mathcal{D}(E=0) \neq 0$ in both the ferromagnetic and spin helix configuration, and self-consistently calculate the LDoS at the center and the edges of the chain. The results are shown in Fig. 4.6, where the solid (dotted) lines correspond to the LDoS at the edges (center) of the chain.

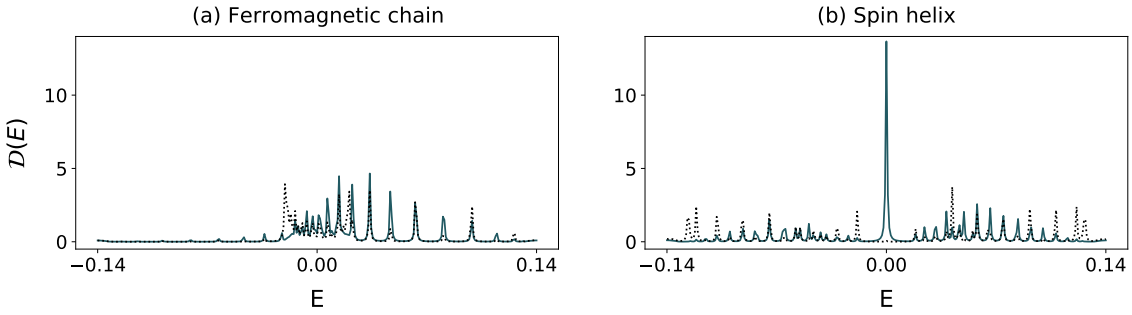

Figure 4.6: Local density of states at the edges (solid lines) and the center (dotted lines) of (a) the ferromagnetic and (b) the spin helix arrangement. The intrinsic linewidth of the energies is taken equal to $\eta = 5 \cdot 10^{-4}$. The bulk gap appears to have vanished in the case of the ferromagnetic chain, however a minigap still exists in the case of the spin helix.

It is crystal clear that the impurity band formed in the case of the ferromagnetic chain leads to the complete closing of the bulk gap. In contrast, a "minigap", which is how we will henceforth refer to the region around zero where $\mathcal{D}(E) = 0$, still exists in the case of the spin helix in the domain $-0.015 \leq E \leq 0.015$ or, equivalently, $-0.11 \lesssim E/\Delta \lesssim 0.11$, as can be seen from the LDoS at the chain's center.

In conclusion, we have identified the non-collinear magnetic chain with $\theta = 2\pi/3$ as a TSC, so what remains to be done is further study this system's properties in both its trivial and topological phase and examine some of the possibilities for experimental realizations.

5 Further Study of the Non-Collinear Magnetic Chain

5.1 Investigation of the $\theta = 2\pi/3$ Spin Helix

In order to understand the conditions for the materialization of the topological non-collinear magnetic chain in realistic situations, we need to investigate more specific aspects of our model system. First of all, we already know that once the closed chain is "cut open", MZMs will be localized at its ends, provided that the value B of the local magnetic field lies in the domain where the system is topologically non-trivial. However, the relative angle between the spins of the impurities at the chain ends may play an important role as far as that domain and the zero-energy peak's height in a LDoS diagram are concerned.

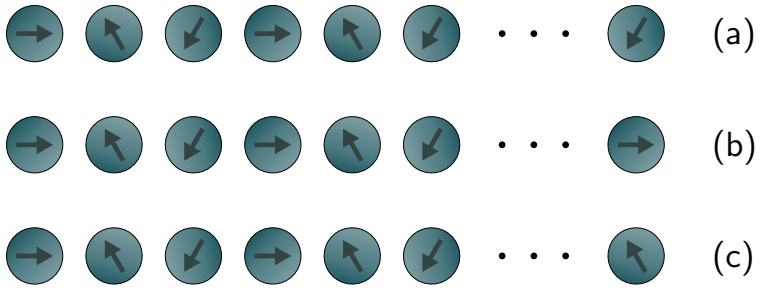

Figure 5.1: The three possible chain arrangements as far as the edge impurities' spins are concerned. Denoting the number of full spin rotations along the chain by the integer ν, (a) corresponds to 3ν, (b) to $3\nu + 1$ and (c) to $3\nu + 2$.

Focusing on the $\theta = 2\pi/3$ spin helix, there are 3 possible configurations for the open chain, with regard to the relative angle of the edge impurities' spins: one where that angle is equal to $4\pi/3$ [Fig. 5.1 (a)], one where the spins are parallel [Fig. 5.1 (b)], and one where that angle is equal to $2\pi/3$ [Fig. 5.1 (c)]. In other words, (a) corresponds to a chain with 3ν impurities, (b) corresponds to a chain with $3\nu + 1$ impurities and (c) corresponds to a chain with $3\nu + 2$ impurities, where ν is the number of full spin rotations along the chain. For each of these cases and taking $\nu = 10$, we calculate the spectral density of the impurities at the chain ends for energies $-0.14 \leq E \leq 0.14$ and values of B in the domain $0.0 \leq B \leq 4.0$ [Fig. 5.2 (a), (c), (e)]. It is clear that there is no significant change in the range of B

for which the system is topological. Choosing $B = 1.8$, a value for which all three chains are in their topological phase, we calculate the LDoS for the impurity atoms at the chain ends [Fig. 5.2 (b), (d), (f) - solid lines], in order to compare the weights of the zero-bias peaks corresponding to the MZMs. In addition to the edge impurities' LDoS, the LDoS corresponding to the pristine host atoms has also been calculated [Fig. 5.2 (b), (d), (f) - dashed lines]. Again, no significant differences can be seen.

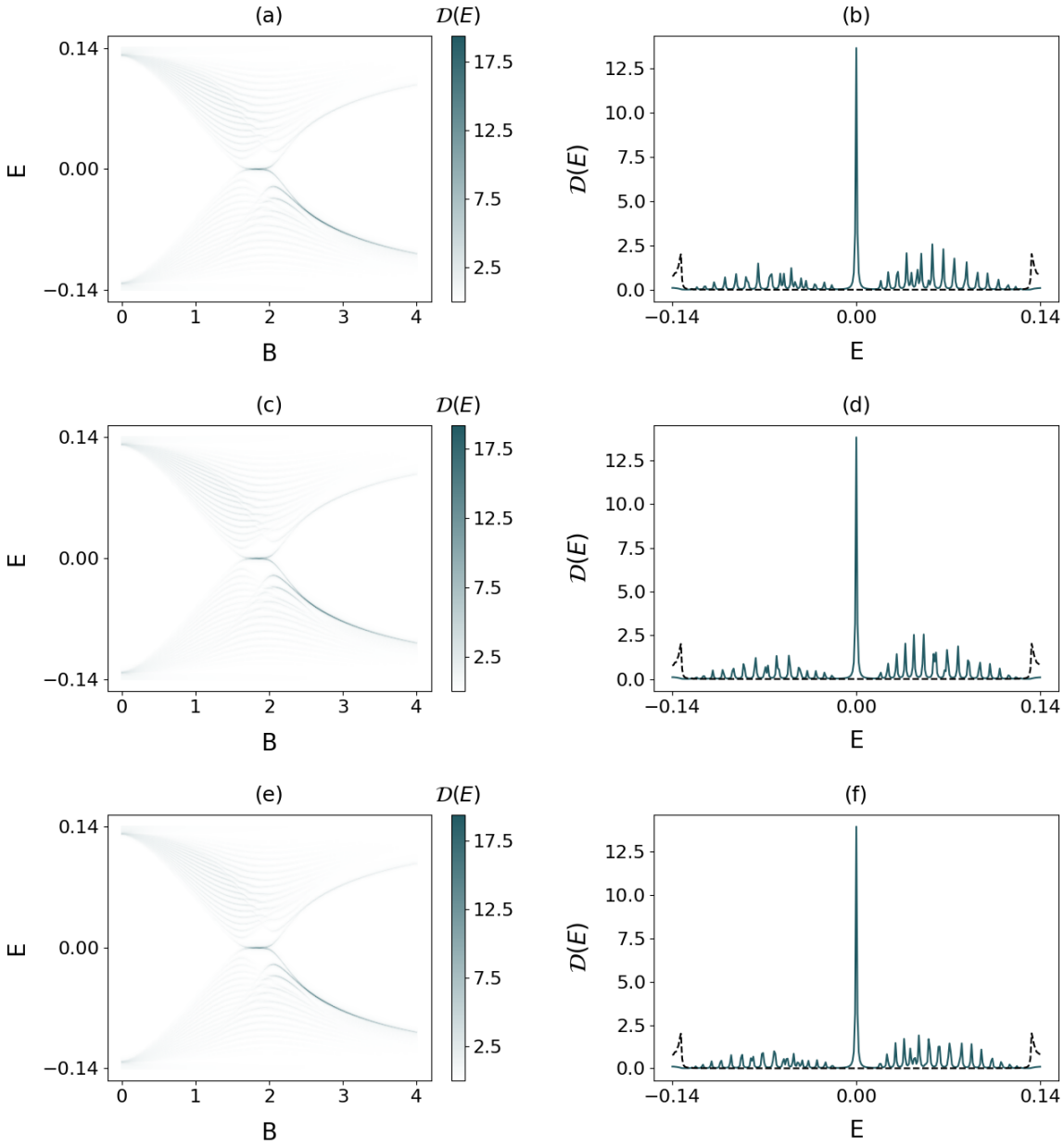

Figure 5.2: Left: Colormap of the edge impurities' spectral density for energies $-0.14 \leq E \leq 0.14$ and local magnetic field magnitudes $0.0 \leq B \leq 4.0$. Right: LDoS for the impurity atoms (solid lines) and the pristine host (dashed lines) at the chain ends, with the intrinsic energy linewidth taken equal to $\eta = 5 \cdot 10^{-4}$. Diagrams (a)-(b), (c)-(d) and (e)-(f) correspond to chains with 30, 31 and 32 impurities, respectively. It appears that the range of B for which the system is topological, the minigap's width around $E = 0$ and the spectral weight of the resonance corresponding to the MZMs is independent of the relative angle of the edge impurity atoms' spins.

Having established the resemblance of the three cases as far as the two points on which we focused are concerned, we choose to work with chains that consist of $3\nu + 1$ atoms. The next task is to study the effect of the chain's total length on the range of B for which the system is topological. For this purpose, we calculate the spectral density of the impurities at the chain ends for the same energies and values of B as in Fig. 5.2, for three different chain sizes: a shorter chain with 31 impurities [Fig. 5.3 (a)], a medium sized chain with 61 impurities [Fig. 5.3 (b)] and a longer chain with 91 impurities [Fig. 5.3 (c)].

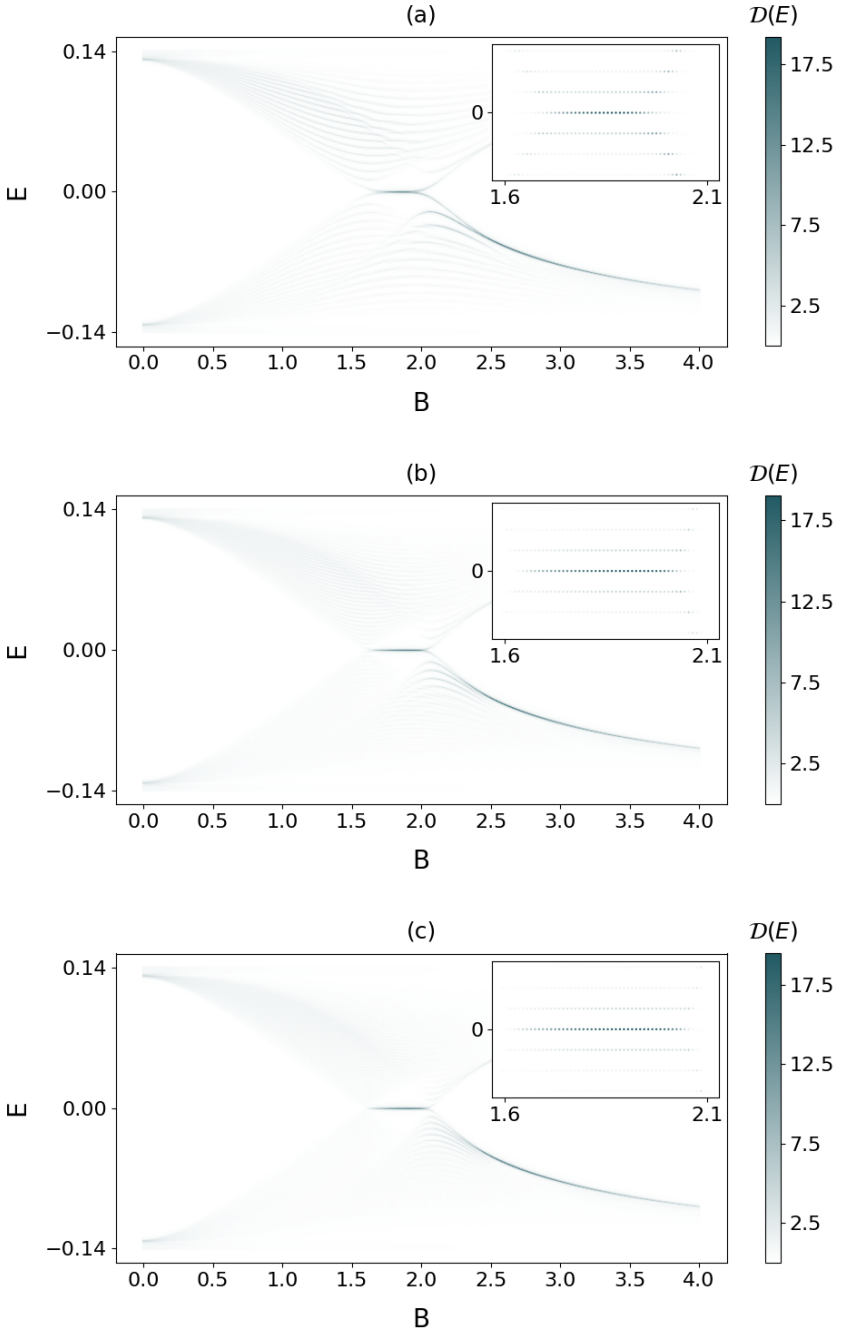

Figure 5.3: Colormaps of the edge impurities' spectral density for energies $-0.14 \leq E \leq 0.14$ and local magnetic field magnitudes $0.0 \leq B \leq 4.0$, for chains with (a) 31 (b) 61 and (c) 91 atoms. The diagram's insets focus on the spectral density at zero energy and the energies shown in the vicinity of $E = 0$ are due to the coarse graining of the energy grid.

One remark that can be made for the three diagrams is that, as the chain's length increases, so does the size of the minigap. The most important observation, however, concerns the domain of B for which the system exhibits a topological phase. As can be seen from the diagrams' insets, where we focus only on energies in the vicinity of zero, an increase in the chain's length leads to an increase in this domain's length. More specifically, the B-domain is $[1.73, 1.93]$ for the 31-atom chain, $[1.66, 2.02]$ for the 61-atom chain and $[1.64, 2.04]$ for the 91-atom chain. This means that as we expand the chain from 31 to 61 atoms, the domain's range increases by 80%. Even though this is significant increase, the corresponding increase in the domain's length is only 11% if the chain is expanded from 61 to 91 atoms. By performing more simulations with chains consisting of up to 121 atoms, we confirmed that, after a point, a saturation appears for the B-domain's length, which remains practically unchanged as we keep adding magnetic atoms to the chain. A point that must be emphasized is that adding more magnetic atoms to the chain significantly increases the corresponding experimental complications: shorter chains are much easier to develop and handle in STM experiments. For this reason, we conclude that the chain consisting of 61 atoms is sufficient in providing us with the desired qualitative results and therefore this is the chain size that will be considered in the following simulations.

5.2 Magnetic Chain Adsorbed on the Surface

So far we have only considered impurities embedded in the host superconductor's surface. In many cases, depending on the experimental method applied, the impurities are deposited on the host surfaces as adatoms, instead of substituting the host atoms[53]. In fact, this is the case in recent experiments performed in order to find evidence of the emergence of MZMs in 1-dimensional TSCs[30,54]. This motivates us to examine how the topological phase of the non-collinear magnetic chain is affected if its constituent atoms are adsorbed on the host superconductor's surface.

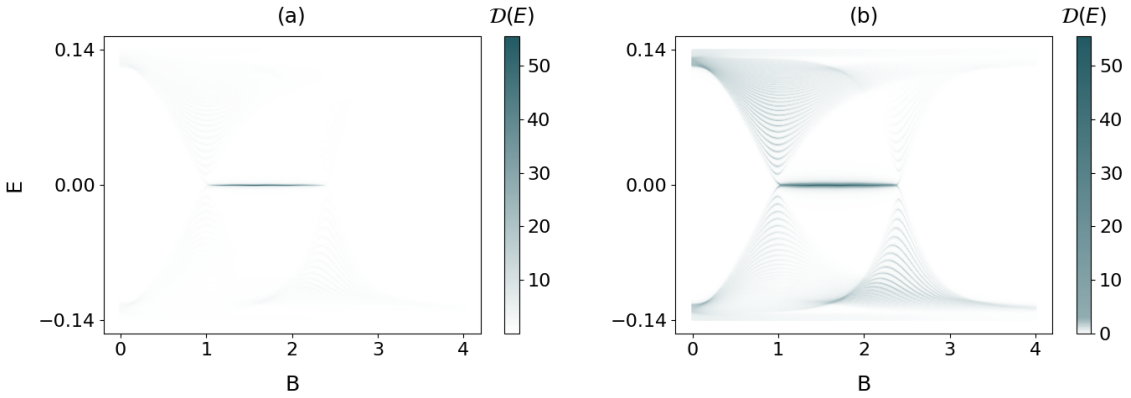

Figure 5.4: Colormaps of the edge impurities' spectral density for energies $-0.14 \leq E \leq 0.14$ and local magnetic field magnitudes $0.0 \leq B \leq 4.0$. The same data have been used for both diagrams, however the midpoint of the colorbar in (b) was taken equal to 3.0 in order for the minigap to be better resolved.

For this purpose, we self-consistently solve the BdG equations for the superconducting slab used in previous simulations (with $\bar{n}_i = 0.4$ for all layers), having first added an additional layer with $\varepsilon = 6.0$, $\Lambda = 0$ and $\bar{n} = 0$ over the topmost superconducting layer. The large value of the self-energy of this layer's atoms (equal to half the energy bandwidth) corresponds to a strong repulsive potential and thus allows us to model the vacuum over the slab. The 61-atom magnetic chain is then embedded in this extra layer along the x-axis and the impurity problem is solved self-consistently. The results of the simulation are shown in Fig. 5.4, which depicts the colormaps of the spectral density for energies lying inside the superconducting gap and values of B taken in the range $0.0 \leq B \leq 4.0$. It is evident that placing the magnetic impurities as adatoms enhances the system's topological phase. The spectral weight of the zero energy modes in the topological phase is almost three times higher compared to the case where the impurity atoms are embedded in the surface [see Fig. 5.3 (b)]. Furthermore, the domain of B for which the system exhibits a topological phase is $[1.03, 2.38]$, meaning that its range is 2.75 times larger than the one for the surface-embedded chain calculated in Section 5.2. Last but not least, the minigap has also increased and almost approaches the bulk gap for the values of B that correspond to the highest spectral weights at $E = 0$. This can be seen in Fig. 5.4 (b), which is the same as Fig. 5.4 (a) with the exception of the colorbar's midpoint taken at 3.0, in order to increase the resolution of the spectral densities at $E \neq 0$.

On one hand, the induced superconductivity in the magnetic chain adsorbed on the surface is suppressed, due to its constituent atoms being more isolated from the superconducting host, compared to the case of the chain embedded in its surface. On the other hand, the induced in-gap states are more localized and thus their interaction with the local magnetic field is stronger. Based on our results, we conclude that the latter effect prevails, since the topological phase appears enhanced.

5.3 Formation of the Spin Helix

Up to this point, we have taken the spin helix configuration of the magnetic chain for granted, without going into detail on how this configuration can be realized in the first place. The two most prominent mechanisms behind the formation of the helical structure are the spin-orbit interaction (SOI)[55,56] and the Ruderman-Kittel-Kasuya-Yosida (RKKY) interaction[57,58] between the magnetic atoms. The former induces an antisymmetric Dzyaloshinskii-Moriya (DM) interaction, while the latter may induce a competition between ferromagnetic and antiferromagnetic behaviour. Experimentally, one way to achieve a strong DM interaction is to interpose a layer of heavy-metal atoms, characterized by a strong SOI, between the host superconductor and the magnetic chain (see Fig. 5.5). On the other hand, such a layer would not be characterized by as strong a superconducting coupling as the Nb substrate.

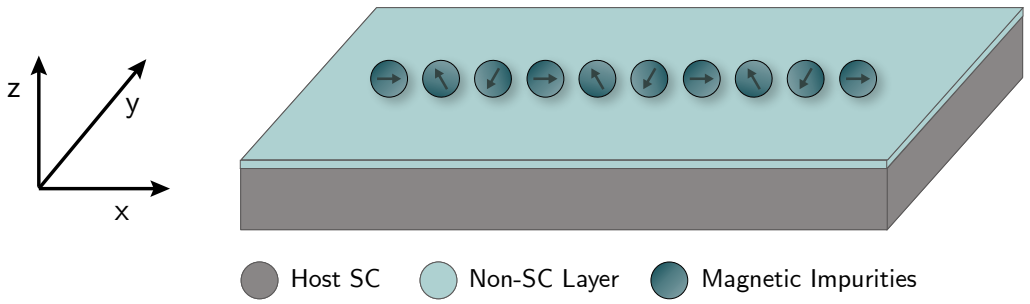

Figure 5.5: Schematic representation of the magnetic impurities as adatoms on a non-superconducting layer placed over the topmost layer of the superconducting slab.

To model this situation, we add an additional layer with $\bar{n} = 0.4$, $\varepsilon = 0$ and $\Lambda = 0$ over the topmost layer of the superconducting slab. Supposing that the slab consists of Nb, the additional layer may be assumed to consist of Ta atoms. Ta is a transition metal with very strong spin-orbit coupling. Its valence electrons occupy d-orbitals, allowing us to keep the same hopping element, and it is isoelectronic to Nb, which is why we do not choose a different value for $\bar{n}$ or ε. Since the critical temperature for the superconducting phase transition of Ta (4.47 K) is lower compared to that of Nb (9.3 K), our assumption of $\Lambda = 0$ can be justified in experiments performed in temperatures in the range $4.47\ \text{K} \leq T \leq 9.3\ \text{K}$[(1)]. After self-consistently solving the BdG equations for the host surface, we introduce the magnetic impurities of the 61-atom chain as adatoms on it, using the method described in Section 5.3, and solve the impurity problem self-consistently. The results for the spectral density for energies inside the superconducting gap and values of B in the range $0.0 \leq B \leq 4.0$ can be seen in the colormap diagrams of Fig. 5.6.

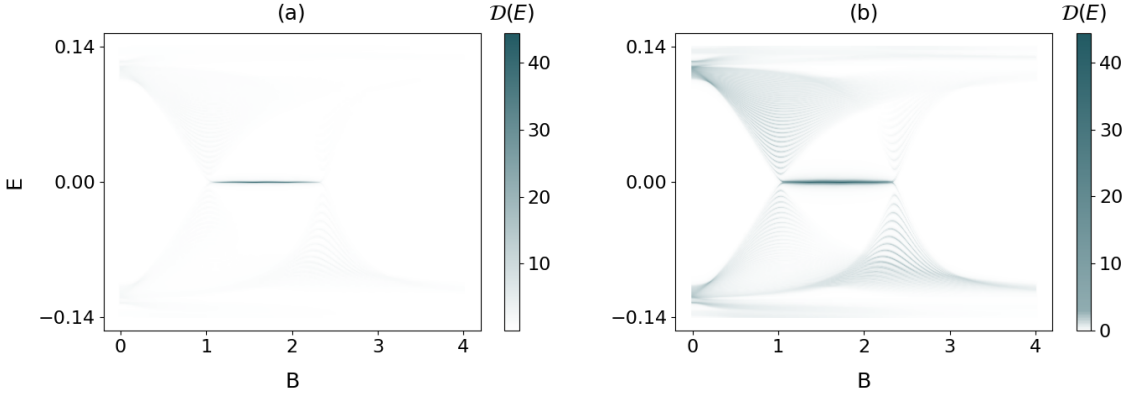

Figure 5.6: Colormaps of the edge impurities' spectral density for energies $-0.14 \leq E \leq 0.14$ and local magnetic field magnitudes $0.0 \leq B \leq 4.0$. The same data have been used for both diagrams, however the midpoint of the colorbar in (b) was taken equal to 3.0 in order for the minigap to be better resolved.

Even though somewhat suppressed compared to the results of Section 5.3, a topological phase still exists for the system and corresponds to $1.07 \leq B \leq 2.36$. This suppression is

(1) Other 5d metals may be used for this purpose, all of which have lower critical temperatures than Nb: Hf ($T_c = 0.38$ K), W ($T_c = 5.5$ K), Re ($T_c = 1.7$ K), Os ($T_c = 0.7$ K), Ir ($T_c = 0.1$ K), Pt ($T_c = 0$ K) [59].

not only indicated by the slightly smaller length of the B-domain, but also by the spectral weight corresponding to $E = 0$. A similar suppression can be seen for the minigap, which is well-resolved in Fig. 5.6 (b), due to our choosing the colorbar's midpoint equal to 3.0. Nonetheless, the fact that the interposed layer does not significantly impact the induced superconductivity in the magnetic chain, as well as the fact that the system still exhibits a topological phase, are very promising for possible experimental realizations.

5.4 Possible Effects of Disorder

Another variable that needs to be considered in this investigation of our model's experimental realization is the fact that, apart from the magnetic atoms that form the non-collinear magnetic chain, additional atoms may be absorbed near the chain, possibly affecting the appearance of MZMs. These additional impurities shall henceforth be referred to as off-chain impurities. The off-chain impurities may assume random positions in the chain's plane, adjacent to the chain's impurity atoms along the y-axis. They are identical to the chain's impurities with the exception that the direction of their local magnetic fields differs by an angle $\pm\theta$ around the y-axis compared to that of their neighbours on the chain. To perform this simulation, we model the system presented in Section 5.3 with 61 atoms in the chain and introduce 10 additional impurities adsorbed on the superconducting surface, in a configuration illustrated in Fig. 5.7.

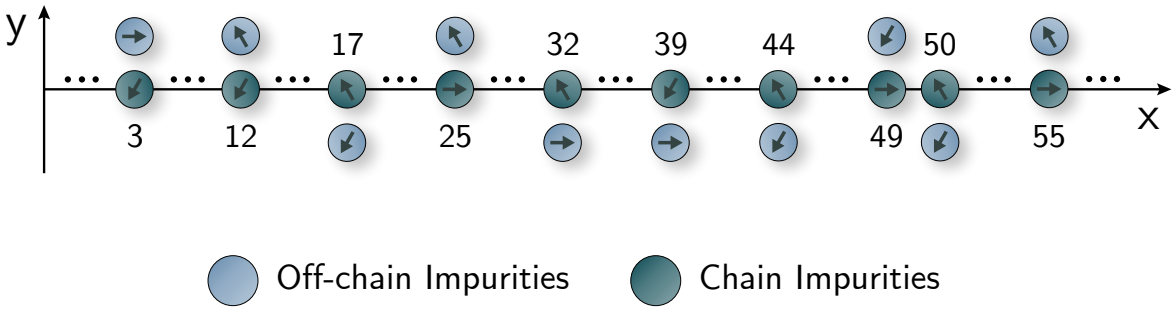

Figure 5.7: Schematic representation of the impurities adsorbed on the superconducting surface. The non-collinear magnetic chain is placed along the x-axis and 10 off-chain impurities are placed at first-neighbour distance along the y-axis next to the chain's impurities.

The results of this simulation are shown in the colormaps of Fig. 5.8, where the intensities correspond to the chain's edge impurities' spectral densities. The effect of the off-chain impurities is evident, since Fig. 5.8 is quite different compared to Fig. 5.4, which corresponds to the isolated magnetic chain. A topological phase clearly still exists for the system for values $1.03 \leq B \leq 1.81$, where the spectral density at $E = 0$ is high and a minigap is present. At $B = 1.82$ the minigap seems to momentarily close and then gradually reopen in the range $1.83 \leq B \leq 2.34$. In this range the spectral density at $E = 0$ is relatively high, but it is about 4 times lower compared to its value in the range $1.03 \leq B \leq 1.81$. Despite that, we

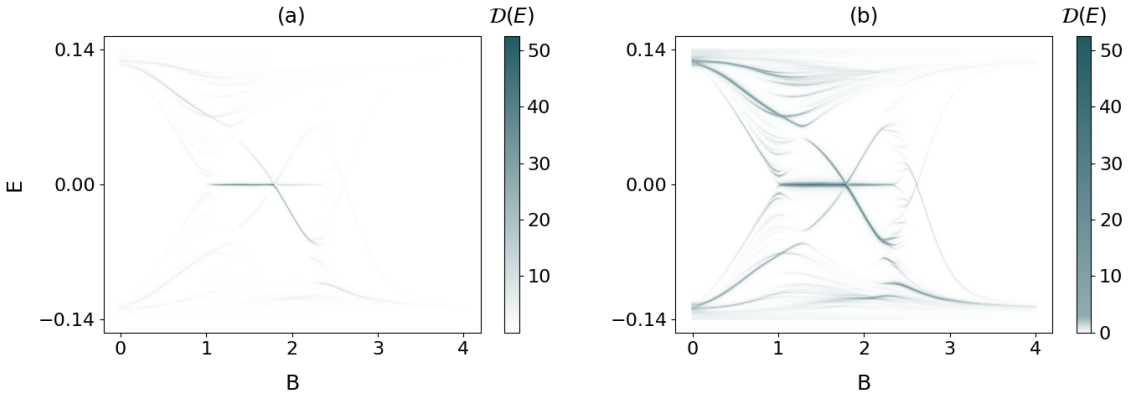

Figure 5.8: Colormaps of the edge impurities' spectral density for energies $-0.14 \leq E \leq 0.14$ and local magnetic field magnitudes $0.0 \leq B \leq 4.0$. The same data have been used for both diagrams, however the midpoint of the colorbar in (b) was taken equal to 3.0.

have shown that, while disorder has a notable impact on the system, the non-collinear chain can still exhibit a topological phase.

5.5 Different Helix Rotation Angles

Even though the results thus far obtained confirm that the non-collinear magnetic chain with $\theta = 2\pi/3$ corresponds to a TSC for values of B that vary depending on the experimental variables studied in the previous sections, a final question that needs to be addressed is whether or not a different choice of θ would yield the same qualitative results. As discussed in Chapter 4, a Majorana number equal to -1 is not definitive proof that a topological superconductor phase exists for the system, since we must additionally confirm that the gap reopens right after the transition $\mathcal{M} \to -1$. Furthermore, for $\theta \neq 2\pi/3$, the periodicity of the spin helix's rotation increases[(2)] and thus a larger supercell has to be defined for the calculation of the Majorana number, which in turns leads to an increase of the required computational time. For these reasons, we choose to evaluate the edge impurities' spectral densities at energies lying in the bulk gap for several values of B, as we've done in all simulations presented in this Chapter, in order to investigate if a phase corresponding to a TSC exists for different helix rotation angles. We choose a chain length of 30 atoms, since we have shown that it is sufficient for the realisation of a topological phase. While simulations were performed for many different values of θ, Fig. 5.9 shows our results for (a) $\theta = \pi/2$, (b) $\theta = \pi/4$, (c) $\theta = \pi/6$ and (d) $\theta = \pi/9$, since they suffice in providing us with a qualitative understanding of how the choice of θ affects the system's topological nature.

Not only do these results confirm that the non-collinear magnetic chain can be realized as a TSC for values of θ other than $2\pi/3$, but they further indicate that decreasing the helix's rotation angle leads to an increase in the length of the topological phase's B-domain, as well as a broadening of the minigap. More specifically, the values of B corresponding to the

[(2)] A full spin rotation along the chain occurs every N consecutive atoms for $\theta = 2\pi/N$.

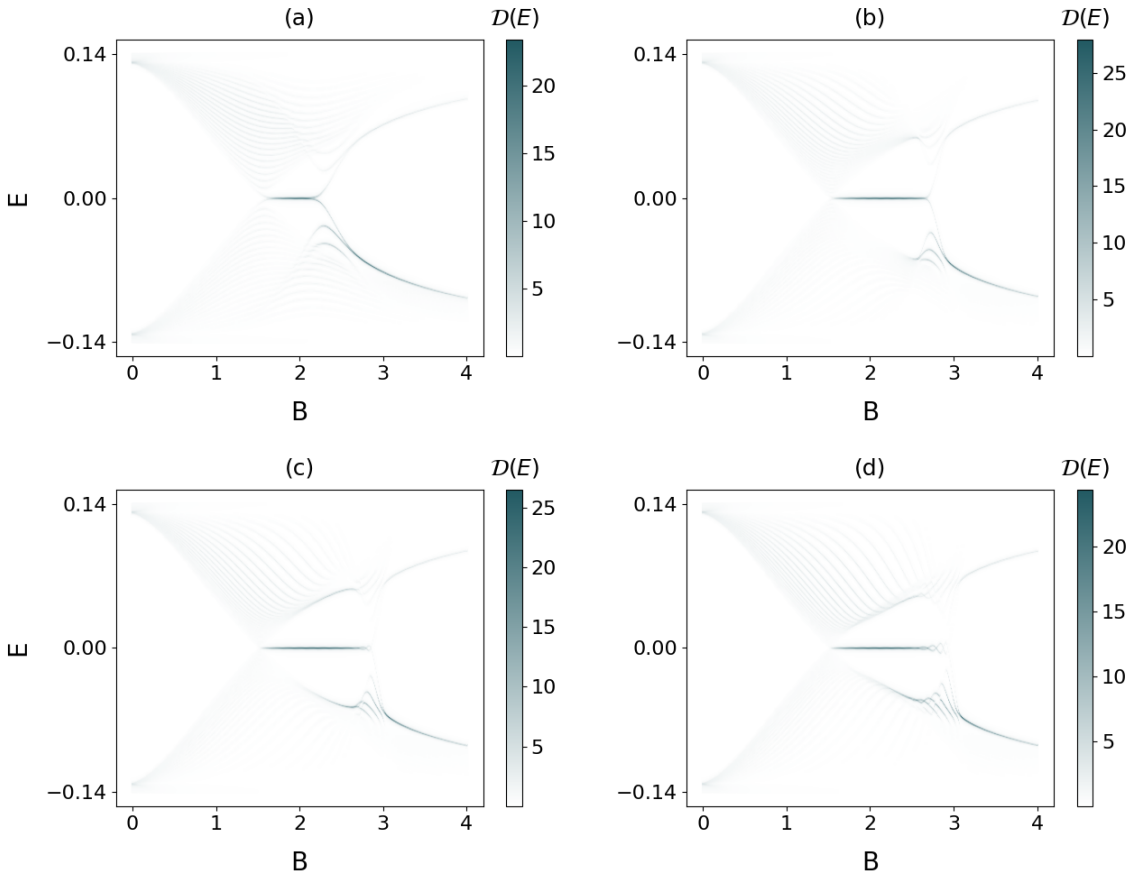

Figure 5.9: Colormaps of the edge impurities' spectral density for energies $-0.14 \leq E \leq 0.14$ and local magnetic field magnitudes $0.0 \leq B \leq 4.0$, for a 30-atom non-collinear magnetic chain. The helix's rotation angle is taken to be (a) $\theta = \pi/2$, (b) $\theta = \pi/4$, (c) $\theta = \pi/6$ and (d) $\theta = \pi/9$. A topological phase is present for all four cases, and the domain of B for which it appear increases as the rotation angle decreases.

topological phase are (a) $1.65 \leq B \leq 2.19$, (b) $1.58 \leq B \leq 2.68$ and (c) $1.56 \leq B \leq 2.75$. For the case $\theta = \pi/9$ the values of B for which the system exhibits a topological phase cannot be clearly determined, due to the crossings-like behaviour of the intensity for $2.52 \leq B \leq 2.89$ in Fig. 5.9 (d). This could be resulting from the fact that in a 30-atom chain, only a single full spin rotation occurs across the chain.

6 Summary and Outlook

In this thesis we studied the effects of impurities embedded in or adsorbed on superconductor surfaces and focused on how they can drive the systems under study into topologically non-trivial superconducting phases. In this final Chapter, we summarize our main results and propose possible paths to future research.

All simulations performed throughout this thesis included the self-consistent solution of the BdG equations for the superconducting host system and Dyson's equation for the impurity problem. The theoretical framework on which our calculations are based was summarized in Chapter 2.

In Chapter 3 we studied single impurities embedded in the surface of superconducting systems. In agreement with literature, we found that non-magnetic impurities induce Friedel-like oscillations for the charge and order parameter, but have no impact on the bulk gap. On the contrary, magnetic impurities lead to the formation of localized in-gap YSR states which appear as double resonances in LDoS diagrams, at energies that depend on the magnetic impurity's local magnetic field's magnitude.

In Chapter 4, following a proposal from the literature, we studied ferromagnetic, antiferromagnetic and spin helix (with helix rotation angle $\theta = 2\pi/3$) configurations for magnetic chains, investigating whether they could exhibit a topologically non-trivial superconducting phase. For this purpose, we calculated each system's Majorana number for various values of the impurities' local magnetic fields' magnitudes, by assuming periodic boundary conditions for the chains. We found that a negative Majorana number appears only for the ferromagnetic and spin helix configurations, however, upon studying the open-chain problem, we realized that the ferromagnetic chain's bulk gap vanishes after the transition and therefore it does not correspond to a topological superconductor. On the other hand, we confirmed the existence of localized MZMs at the chain's edges for the spin helix configuration, signalled by their high spectral densities at zero energy in LDoS diagrams, which are protected by the minigap that is formed inside the bulk gap, in the vicinity of $E = 0$.

Having identified the non-collinear magnetic chain with helix rotation angle $\theta = 2\pi/3$ as a 1-dimensional TSC, in Chapter 5 we explored variables that could affect the system's topological phase. As far as the chain's length is concerned, we found that longer chains lead to larger domains of B for which the system's phase is topologically non-trivial, however

after a specific length this effect is saturated. Then, we studied the case where the magnetic chain is adsorbed on the superconducting surface and discovered that the topological phase is significantly enhanced compared to the case where the chain is embedded in the surface. In order to account for some of the experimental conditions leading to the formation of the spin helix, we interposed a layer of vanishing superconducting coupling between the superconducting surface and the chain. This is meant to model a heavy-metal layer that, in experiment, induces strong anisotropic exchange in the chain due to its strong SOI. Our findings indicated that, while superconductivity is slightly suppressed for the magnetic chain, a topologically non-trivial phase still exists for the system. We also studied the possible effects of disorder by introducing additional off-chain impurities. The addition of these impurities led to a decrease in the length of the B-domain for which the system exhibits a topological phase. Nonetheless, MZMs still appeared at the chain's edges, indicating that the realization of the spin helix topological superconductor does not require ideal experimental conditions. Finally, we explored what happens if the spin helix's rotation angle assumes values other than $2\pi/3$ and found that smaller rotation angles lead to an enhancement of the topological phase.

Based on our results, we conclude that the non-collinear magnetic chain embedded on a superconductor surface provides a good hunting ground for the experimental confirmation of the emergence of Majorana quasiparticles in TSCs. While signatures of MZMs have already been observed as zero-bias peaks in STM measurements [27–30], the definitive proof of their existence may come from the observation of their non-Abelian exchange statistics. While our studied system corresponds to a 1-dimensional TSC and the concept of exchange statistics is ill-defined in 1 dimension [14], this obstacle can be overcome by fabricating networks of 1-dimensional TSCs [60].

As far as possible future theoretical extensions to our model are concerned, the study of Y-shaped magnetic chains, as well as simulations with two or more chains, might contribute to the experimental fabrication of such networks. Furthermore, deviations from the ideal case of the spin helix arrangement can be investigated, for example by further exploring the impact of disorder on the topological phase, or by considering non-uniform rotation angles for the spin helix. Finally, our simulations can be augmented in the future by employing the more realistic, but numerically more complicated, BdG density-functional method [61,62], in order to achieve a better prediction of experimental results.

Appendix

A.1 Self-Consistency Schemes

The self-consistency scheme applied for the calculations of the system's normal state properties can be seen in Fig. A.1.

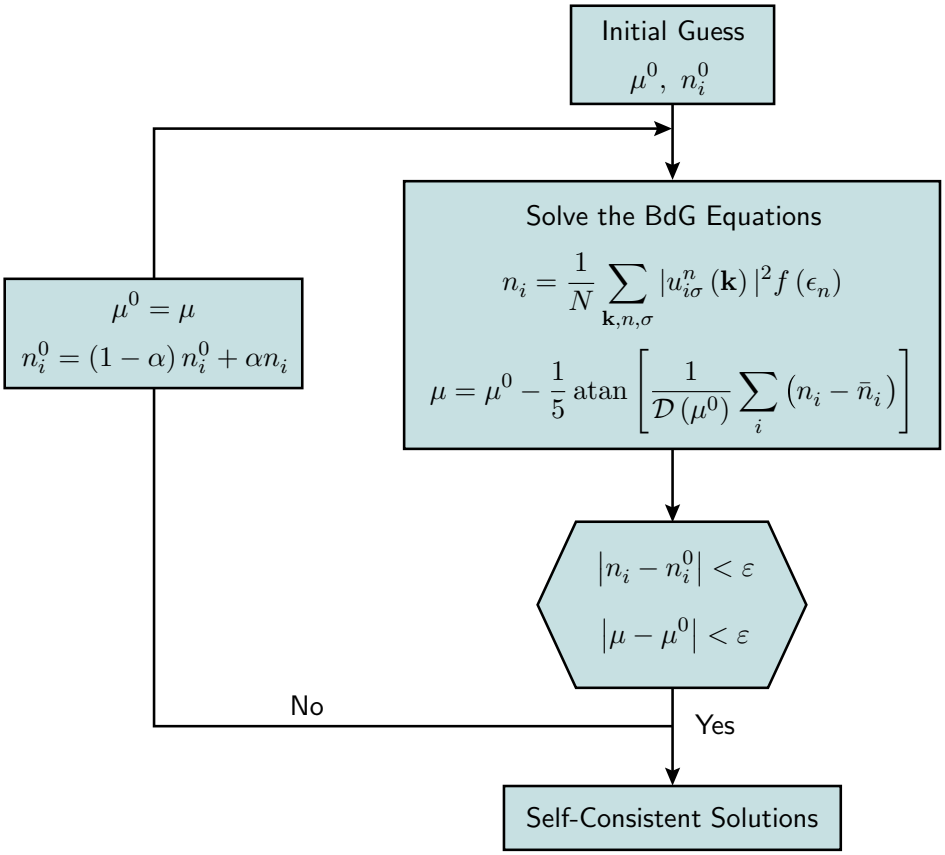

Figure A.1: Self-consistency scheme for the calculations of the normal state.

Instead of a fixed chemical potential, our code's inputs are the desired values for the atomic charges, $\bar{n}_i$. An initial guess μ^0 and n_i^0 is made for the chemical potential and the atomic charges, respectively, and the BdG Hamiltonian is diagonalized. Its eigenvectors and eigenvalues are used in order to compute the new charges and the new chemical potential as

$$\mu = \mu^0 - \frac{1}{5}\operatorname{atan}\left[\frac{1}{\mathcal{D}(\mu^0)}\sum_i (n_i - \bar{n}_i)\right], \tag{A.1}$$

where $\mathcal{D}\left(\mu^0\right)$ is the density of states summed over all atoms at energy equal to μ^0. This empirical expression ensures that the system's total desired charge corresponds to the correct

chemical potential and the arctangent term is inserted to avoid big jumps for the chemical potential between iterations. If the difference between the initial and new values of the chemical potential and each charge is not higher than ε, then convergence has been achieved. Otherwise, the process is repeated with the input chemical potential equal to the one calculated by Eq. (A.1) and the input charges given by a linear mixing[(1)] of their initial and new values. For all simulations we choose $\varepsilon = 10^{-4}$ and $\alpha = 0.1$.

Once convergence is achieved for the normal state, we proceed to the superconducting state's calculations. The corresponding self-consistency scheme can be seen in Fig. A.2. For the first iteration, an initial guess Δ_i^0 is made for the order parameters, while the input charges are set equal to the converged values from the normal state's calculations. A similar convergence criterion is inserted, except this time it is stricter, i.e., $\varepsilon = 10^{-5}$. The input values of the charges and order parameters for the following iterations are once again calculated by a linear mixing and in most cases $\alpha = \beta = 0.1$ are chosen.

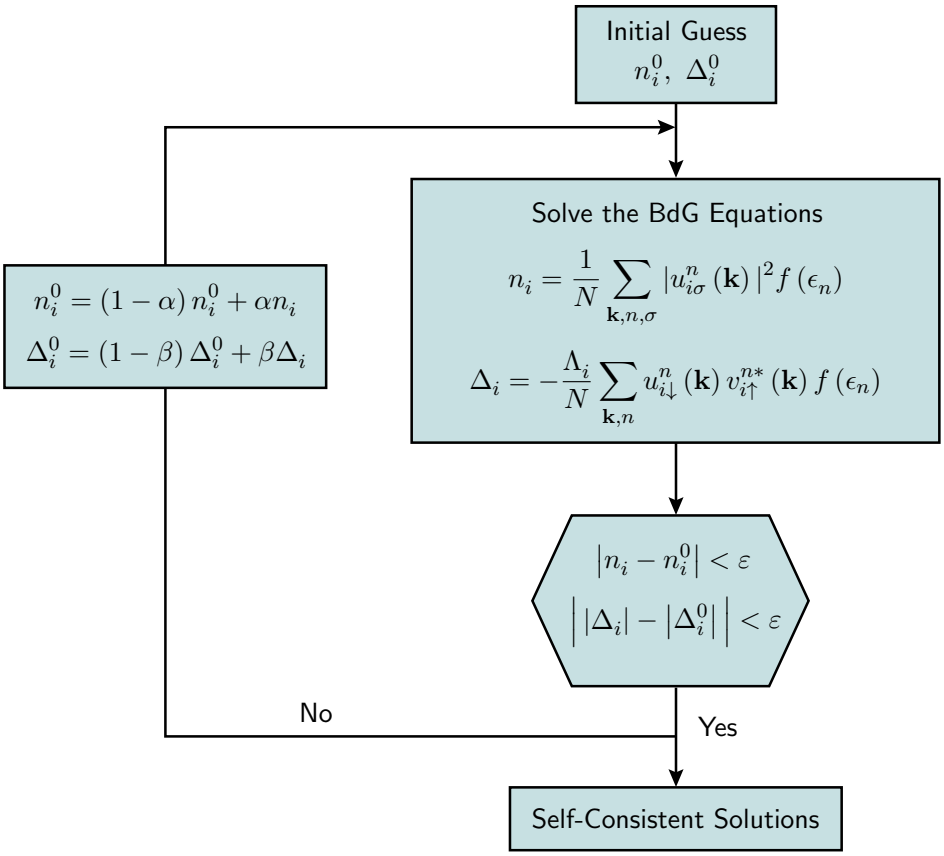

Figure A.2: Self-consistency scheme for the calculations of the superconducting state.

The converged values for the charges and order parameters correspond to the host system. Once the system is perturbed by the addition of impurities, the Green functions formalism has to be applied, so a third self-consistency scheme is introduced during the solution of Dyson's equation. This is depicted in Fig. A.3. For the first iteration, the values for the

(1) Even though it converges slowly, compared to other methods, the choice of linear mixing was made because of its stability. An alternative for faster convergence would be Broyden mixing [63].

charges and the order parameters are taken equal for both the host and impurity atoms. From the second iteration onwards, a mixing occurs for the impurity atoms' charges and order parameters, using the calculations of the previous iteration. For the purposes of our simulations, we set the mixing parameters equal to $\alpha = \beta = 1.0$, since the process converges rather fast. The convergence criterion is again $\varepsilon = 10^{-5}$.

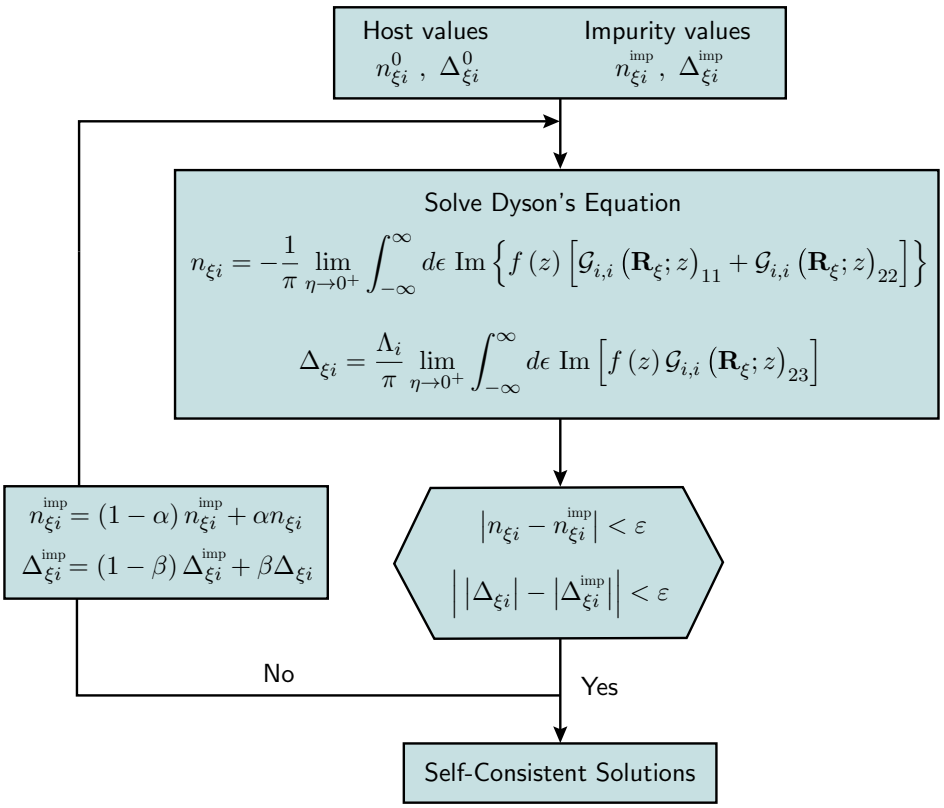

Figure A.3: Self-consistency scheme for the impurity problem.

A.2 Modelling a Slab

In order to study surfaces and still take advantage of the computational simplifications that Bloch's theorem provides, we set up the system on a 3-dimensional cubic lattice. The lattice's symmetry allows us to model the problem of $x - y$ periodic layers stacked along the z-axis (a structure known as a slab) as an effective 3-dimensional periodic system, by defining a supercell consisting of equidistant atoms along the z-axis (see Fig. A.4). The slab should be thick enough in order to minimize the interaction between the top and bottom layers. If the unit vector along the z-axis is taken equal to the thickness of the slab, we end up with a regular cubic lattice, since we have simply "glued" together a number of slabs. However, we can separate them by taking that unit vector sufficiently large, thus creating an effective vacuum and ensuring that no interaction occurs between adjacent slabs.

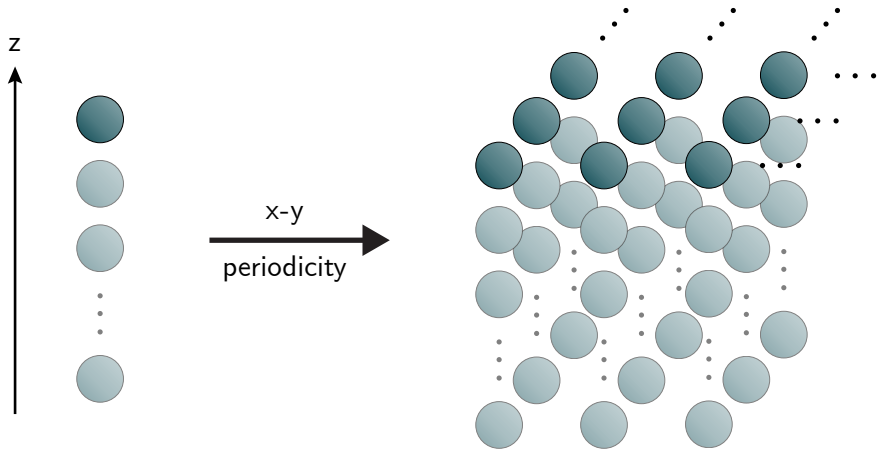

Figure A.4: Modelling a slab using a 3-dimensional periodic cubic lattice.

A.3 Majorana Number Calculation

In order to model the host superconductor and the impurities embedded on its surface as a 1-dimensional periodic system, we first solve the BdG equations self-consistently for N layers along the z-axis that are periodic on the $x-y$ plane. Then, we construct a supercell as follows: depending on the spin periodicity of the magnetic chain, we place X magnetic atoms along the x-axis. In the cases studied in Section 4.3, $X = 1$ for the ferromagnetic chain, $X = 2$ for the antiferromagnetic chain and $X = 3$ for the spin helix. Then, host atoms are placed along the y-axis, so that each magnetic impurity has Y host atoms to its left and Y host atoms to its right, thus creating a 2-dimensional layer. Finally, additional host layers are added under the layer containing the magnetic impurities, so that there is a total of Z layers, where Z is an even number. As a result, the supercell consists of $X(2Y + 1)Z$ atoms. For the host atoms on the first $Z/2$ layers, we use the self-consistent solutions of the BdG equations corresponding to the first $Z/2$ layers of the N layer problem, while for the host atoms on the rest layers we use the self-consistent solutions of the BdG equations corresponding to the bottom $Z/2$ layers of the N layer problem.

For the cases studied in Section 4.3, we chose $N = 100$, $Y = 10$ and $Z = 20$. The Pfaffians required for the calculation of the Majorana number are computed using the blocked version of the Parlett-Reid algorithm, implemented for FORTRAN by M. Wimmer [52]. The time required for the computation of each Majorana number scales as $\propto Z^3$, therefore the computational time required for the calculations in the case $Z = N$ would be very large. Of course, choosing $Z \neq N$ may contribute to the fact that the domain of B for which a topological phase appears from the calculations of the Majorana number has a larger length compared to the domain corresponding to the open chain problem. However, the main reason for the different results remains the fact that the open chain's length is finite.

References

[1] L. D. Landau. The theory of a fermi liquid. *Soviet Physics JETP*, 3:920–925, 1957. DOI: http://www.jetp.ac.ru/files/Landau1en.pdf.

[2] E. M. Lifshitz and L. P. Pitaevskii. *Statistical Physics: Theory of the Condensed State (Course of Theoretical Physics Vol. 9)*. Pergamon Press, 1980.

[3] J. Bardeen, L. N. Cooper, and J. R. Schrieffer. Theory of superconductivity. *Phys. Rev.*, 108:1175–1204, 1957. DOI: https://doi.org/10.1103/PhysRev.108.1175.

[4] V. L. Ginzburg and L. D. Landau. On the theory of superconductivity. *Zh. Eksp. Teor. Fiz.*, 20, 1950. DOI: https://doi.org/10.1016/B978-0-08-010586-4.50078-X.

[5] K. von Klitzing, G. Dorda, and M. Pepper. New method for high-accuracy determination of the fine-structure constant based on quantized hall resistance. *Phys. Rev. Lett.*, 45: 494–497, 1980. DOI: https://doi.org/10.1103/PhysRevLett.45.494.

[6] D. J. Thouless, M. Kohmoto, M. P. Nightingale, and M. den Nijs. Quantized hall conductance in a two-dimensional periodic potential. *Phys. Rev. Lett.*, 49:405–408, 1982. DOI: https://doi.org/10.1103/PhysRevLett.49.405.

[7] T. D. Stanescu. *Introduction to Topological Quantum Matter & Quantum Computation.* CRC Press, 2016.

[8] C. L. Kane and E. J. Mele. Z_2 topological order and the quantum spin hall effect. *Phys. Rev. Lett.*, 95:146802, 2005. DOI: https://doi.org/10.1103/PhysRevLett.95.146802.

[9] M. König, S. Wiedmann, C. Brüne, A. Roth, H. Buhmann, L. W. Molenkamp, X.-L. Qi, and S.-C. Zhang. Quantum spin hall insulator state in hgte quantum wells. *Science*, 318:766–770, 2007. DOI: https://doi.org/10.1126/science.1148047.

[10] S.-Y. Xu, I. Belopolski, N. Alidoust, M. Neupane, et al. Discovery of a Weyl fermion semimetal and topological fermi arcs. *Science*, 349:613–617, 2015. DOI: https://doi.org/10.1126/science.aaa9297.

[11] M. Sato and Y. Ando. Topological superconductors: a review. *Rep. Prog. Phys.*, 80, 2017. DOI: https://doi.org/10.1088/1361-6633/aa6ac7.

[12] E. Majorana. Teoria simmetrica dell'elettrone e del positrone. *Nuovo Cimento*, 5: 171–184, 1937. DOI: https://doi.org/10.1007/BF02961314.

[13] F. Wilczek. Majorana returns. *Nature Physics*, 5:614–618, 2009. DOI: https://doi.org/10.1038/nphys1380.

[14] C. Nayak, S. H. Simon, A. Stern, M. Freedman, and S. Das Sarma. Non-Abelian anyons and topological quantum computation. *Rev. Mod. Phys.*, 80:1083–1159, 2008. DOI: https://doi.org/10.1103/RevModPhys.80.1083.

[15] C. W. J. Beenakker. Search for Majorana fermions in superconductors. *Annual Review of Condensed Matter Physics*, 4:113–136, 2013. DOI: https://doi.org/10.1146/annurev-conmatphys-030212-184337.

[16] L. Fu and C. L. Kane. Superconducting proximity effect and Majorana fermions at the surface of a topological insulator. *Phys. Rev. Lett.*, 100:096407, 2007. DOI: https://doi.org/10.1103/PhysRevLett.100.096407.

[17] J. D. Sau, R. M. Lutchyn, S. Terawi, and S. Das Sarma. Generic new platform for topological quantum computation using semiconductor heterostructures. *Phys. Rev. Lett.*, 104:040502, 2010. DOI: https://doi.org/10.1103/PhysRevLett.104.040502.

[18] R. M. Lutchyn, J. D. Sau, and S. Das Sarma. Majorana fermions and a topological phase transition in semiconductor-superconductor heterostructures. *Phys. Rev. Lett.*, 105:077001, 2010. DOI: https://doi.org/10.1103/PhysRevLett.105.077001.

[19] Y. Oreg, G. Refael, and F. von Oppen. Helical liquids and Majorana bound states in quantum wires. *Phys. Rev. Lett.*, 105:177002, 2010. DOI: https://doi.org/10.1103/PhysRevLett.105.177002.

[20] S. Diehl, E. Rico, M. A. Baranov, and P. Zoller. Topology by dissipation in atomic quantum wires. *Nature Physics*, 7:971–977, 2011. DOI: https://doi.org/10.1038/nphys2106.

[21] S. Gangadharaiah, B. Braunecker, P. Simon, and D. Loss. Majorana edge states in interacting one-dimensional systems. *Phys. Rev. Lett.*, 107:036801, 2011. DOI: https://doi.org/10.1103/PhysRevLett.107.036801.

[22] L. Fidkowski, R. M. Lutchyn, C. Nayak, and M. P. A. Fisher. Majorana zero modes in one-dimensional quantum wires without long-ranged superconducting order. *Phys. Rev. B*, 84:195436, 2011. DOI: https://doi.org/10.1103/PhysRevB.84.195436.

[23] T.-P. Choy, J. M. Edge, A. R. Akhmerov, and C. W. J. Beenakker. Majorana fermions emerging from magnetic nanoparticles on a superconductor without spin-orbit coupling. *Phys. Rev. B.*, 84:195442, 2011. DOI: https://doi.org/10.1103/PhysRevB.84.195442.

[24] J. D. Sau and S. Das Sarma. Realizing a robust practical Majorana chain in a quantum-dot-superconductor linear array. *Nature Communications*, 3, 2012. DOI: https://doi.org/10.1038/ncomms1966.

[25] I. Martin and A. F. Morpurgo. Majorana fermions in superconducting helical magnets. *Phys. Rev. B.*, 85:144505, 2012. DOI: https://doi.org/10.1103/PhysRevB.85.144505.

[26] S. Nadj-Perge, I. K. Drozdov, B. A. Bernevig, and A. Yazdani. Proposal for realizing Majorana fermions in chains of magnetic atoms on a superconductor. *Phys. Rev. B*, 88: 020407, 2013. DOI: https://link.aps.org/doi/10.1103/PhysRevB.88.020407.

[27] V. Mourik, K. Zuo, S. M. Frolov, S. R. Plissard, E. P. A. M. Bakkers, and L. P. Kouwenhoven. Signatures of Majorana fermions in hybrid superconductor-semiconductor nanowire devices. *Science*, 336:1003–1007, 2012. DOI: https://doi.org/10.1126/science.1222360.

[28] A. Das, Y. Ronen, Y. Most, Y. Oreg, M. Heiblum, and H. Shtrikman. Zero-bias peaks and splitting in an Al–InAs nanowire topological superconductor as a signature of Majorana fermions. *Nature Physics*, 8:887–895, 2012. DOI: https://doi.org/10.1038/nphys2479.

[29] M. T. Deng, C. L. Yu, G. Y. Huang, M. Larsson, P. Caroff, and H. Q. Xu. Anomalous zero-bias conductance peak in a Nb–InSb nanowire–Nb hybrid device. *Nano Lett.*, 12: 6414–6419, 2012. DOI: https://doi.org/10.1021/nl303758w.

[30] S. Nadj-Perge, I. K. Drozdov, J. Li, H Chen, S. Jeon, J. Seo, A. H. MacDonald, B. A. Bernevig, and A. Yazdani. Observation of Majorana fermions in ferromagnetic atomic chains on a superconductor. *Science*, 364:602–607, 2014. DOI: https://doi.org/10.1126/science.1259327.

[31] P. Hohenberg and W. Kohn. Inhomogeneous electron gas. *Phys. Rev.*, 136:B864–B871, 1964. DOI: https://link.aps.org/doi/10.1103/PhysRev.136.B864.

[32] W. Kohn and L. J. Sham. Self-consistent equations including exchange and correlation effects. *Phys. Rev.*, 140:A1133–A1138, 1965. DOI: https://link.aps.org/doi/10.1103/PhysRev.140.A1133.

[33] N. N. Bogoliubov. On a new method in the theory of superconductivity. *Il Nuovo Cimento (1955-1965)*, 7:794–805, 1958. DOI: https://doi.org/10.1007/BF02745585.

[34] P. G. de Gennes. *Superconductivity of metals and alloys.* CRC Press, 1999.

[35] J. F. Annett. *Superconductivity, Superfluids and Condensates.* Oxford University Press, 2004.

[36] T. G. Saunderson, J. F. Annett, B. Újfalussy, G. Csire, and M. Gradhand. Gap anisotropy in multiband superconductors based on multiple scattering theory. *Phys. Rev. B*, 101:064510, 2020. DOI: https://doi.org/10.1103/PhysRevB.101.064510.

[37] S. Y. Savrasov and D. Y. Savrasov. Electron-phonon interactions and related physical properties of metals from linear-response theory. *Phys. Rev. B*, 54:16487 – 16501, 1996. DOI: https://doi.org/10.1103/PhysRevB.54.16487.

[38] A. L. Fetter. Spherical impurity in an infinite superconductor. *Phys. Rev.*, 140:1921–1936, 1965. DOI: https://doi.org/10.1103/PhysRev.140.A1921.

[39] A. V. Balatsky, I. Vekhter, and J.-X. Zhu. Impurity-induced states in conventional and unconventional superconductors. *Rev. Mod. Phys.*, 78:373–433, 2006. DOI: https://doi.org/10.1103/RevModPhys.78.373.

[40] B. W. Heinrich, J. I. Pascual, and K. J. Franke. Single magnetic adsorbates on s-wave superconductors. *Progress in Surface Science*, 93:1–19, 2018. DOI: https://doi.org/10.1016/j.progsurf.2018.01.001.

[41] L. Yu. Bound state in superconductors with paramagnetic impurities. *Acta Phys. Sin.*, 21:75–91, 1965. DOI: https://doi.org/10.7498/aps.21.75.

[42] H. Shiba. Classical spins in superconductors. *Progress of Theoretical Physics*, 40:435–451, 1968. DOI: https://doi.org/10.1143/PTP.40.435.

[43] A. I. Rusinov. On the theory of gapless superconductivity in alloys containing paramagnetic impurities. *Soviet Physics JETP*, 29:1101–1106, 1969. DOI: http://www.jetp.ac.ru/cgi-bin/e/index/e/29/6/p1101?a=list.

[44] M. I. Salkola, A. V. Balatsky, and J. R. Schrieffer. Spectral properties of quasiparticle excitations induced by magnetic moments in superconductors. *Phys. Rev. B*, 55:12648–12661, 1997. DOI: https://doi.org/10.1103/PhysRevB.55.12648.

[45] A. A. Khajetoorians, B. Baxevanis, C. Hübner, T. Schlenk, S. Krause, T. O. Wehling, S. Lounis, A. Lichtenstein, D. Pfannkuche, J. Wiebe, and R. Wiesendanger. Current-driven spin dynamics of artificially constructed quantum magnets. *Science*, 339:55–59, 2013. DOI: https://doi.org/10.1126/science.1228519.

[46] S. Yan, L. Malavolti, J. A. J. Burgess, A. Droghetti, A. Rubio, and S. Loth. Nonlocally sensing the magnetic states of nanoscale antiferromagnets with an atomic spin sensor. *Sci. Adv.*, 3, 2017. DOI: https://dx.doi.org/10.1126/sciadv.1603137.

[47] S. Loth, S. Baumann, C. P. Lutz, D. M. Eigler, and A. J. Heinrich. Bistability in atomic-scale antiferromagnets. *Science*, 335:196–199, 2012. DOI: https://doi.org/10.1126/science.1214131.

[48] A. Y. Kitaev. Unpaired Majorana fermions in quantum wires. *Phys. Usp.*, 44:131–136, 2001. DOI: https://dx.doi.org/10.1070/1063-7869/44/10S/S29.

[49] A. Altland and M. R. Zirnbauer. Nonstandard symmetry classes in mesoscopic normal-superconducting hybrid structures. *Phys. Rev. B*, 55:1142–1161, 1997. DOI: https://doi.org/10.1103/PhysRevB.55.1142.

[50] S. Ryu, A. P. Schnyder, A. Furusaki, and A. W. W. Ludwig. Topological insulators and superconductors: Tenfold way and dimensional hierarchy. *New Journal of Physics*, 12: 065010, 2010. DOI: https://doi.org/10.1088/1367-2630/12/6/065010.

[51] J. C. Budich and E. Ardonne. Equivalent topological invariants for one-dimensional Majorana wires in symmetry class D. *Phys. Rev. B*, 88:075419, 2013. DOI: https://doi.org/10.1103/PhysRevB.88.075419.

[52] M. Wimmer. Algorithm 923: Efficient numerical computation of the pfaffian for dense and banded skew-symmetric matrices. *ACM Transactions on Mathematical Software*, 38:30, 2012. DOI: https://doi.org/10.1145/2331130.2331138.

[53] R. Wiesendanger. Spin mapping at the nanoscale and atomic scale. *Rev. Mod. Phys.*, 81:1495–1550, 2009. DOI: https://doi.org/10.1103/RevModPhys.81.1495.

[54] M. Ruby, F. Pientka, Y. Peng, F. von Oppen, B. W. Heinrich, and K. J. Franke. End states and subgap structure in proximity-coupled chains of magnetic adatoms. *Phys. Rev. Lett.*, 115:197204, 2015. DOI: https://doi.org/10.1103/PhysRevLett.115.197204.

[55] M. Menzel, Y. Mokrousov, R. Wieser, J. E. Bickel, E. Vedmedenko, S. Blügel, S. Heinze, K. von Bergmann, A. Kubetzka, and R. Wiesendanger. Information transfer by vector spin chirality in finite magnetic chains. *Phys. Rev. Lett.*, 108:197204, 2012. DOI: https://doi.org/10.1103/PhysRevLett.108.197204.

[56] A. Fert, V. Cros, and J. Sampaio. Skyrmions on the track. *Nature Nanotechnology*, 8: 152–156, 2013. DOI: https://doi.org/10.1038/nnano.2013.29.

[57] B. Braunecker and P. Simon. Interplay between classical magnetic moments and superconductivity in quantum one-dimensional conductors: Toward a self-sustained topological Majorana phase. *Phys. Rev. Lett.*, 111:147202, 2013. DOI: https://doi.org/10.1103/PhysRevLett.111.147202.

[58] J. Klinovaja, P. Stano, A. Yazdani, and D. Loss. Topological superconductivity and Majorana fermions in RKKY systems. *Phys. Rev. Lett.*, 111:186805, 2013. DOI: https://doi.org/10.1103/PhysRevLett.111.186805.

[59] C. Buzea and K. Robbie. Assembling the puzzle of superconducting elements: a review. *Supercond. Sci. Technol.*, 18:R1–R8, 2005. DOI: http://dx.doi.org/10.1088/0953-2048/18/1/R01.

[60] J. Alicea, Y. Oreg, G. Refael, F. von Oppen, and M. P. A. Fisher. Non-Abelian statistics and topological quantum information processing in 1D wire networks. *Nature Physics*, 7:412–417, 2011. DOI: https://doi.org/10.1038/nphys1915.

[61] M. B. Suvasini and B. L. Gyorffy. A multiple scattering method for solving Bogoliubov-de Gennes equations of superconductivity. *Physica C*, 195:109–126, 1992. DOI: https://doi.org/10.1016/0921-4534(92)90081-M.

[62] M. B. Suvasini, W. M. Temmerman, and B. L. Gyorffy. Computational aspects of density-functional theories of superconductors. *Phys. Rev. B*, 48:1202–1210, 1993. DOI: https://doi.org/10.1103/PhysRevB.48.1202.

[63] C. G. Broyden. A class of methods for solving nonlinear simultaneous equations. *Mathematics of Computation*, 19:577–593, 1965. DOI: https://doi.org/10.1090/S0025-5718-1965-0198670-6.

[64] J.-X. Zhu. *Bogoliubov-de Gennes Method and Its Applications*. Springer, 2016.

[65] L. Lauke, M. S. Scheurer, A. Poenicke, and J. Schmalian. Friedel oscillations and Majorana zero modes in inhomogeneous superconductors. *Phys. Rev. B*, 98:134502, 2018. DOI: https://doi.org/10.1103/PhysRevB.98.134502.

[66] C. W. J. Beenakker. Random-matrix theory of Majorana fermions and topological superconductors. *Rev. Mod. Phys.*, 87:1037–1066, 2015. DOI: https://doi.org/10.1103/RevModPhys.87.1037.